SAND80-0454
Unlimited Release

(1)

Geologic Flow Characterization Using Tracer Techniques

Robert D. Klett, Craig E. Tyner, Eugene S. Hertel, Jr

Prepared by Sandia National Laboratories, Albuquerque, New Mexico 87185
and Livermore, California 94550 for the United States
Department of Energy under Contract DE-AC04-76DP00789

Printed April 1981

Sandia National Laboratories

SF 2900-Q(3-80)

DISCLAIMER

Issued by Sandia National Laboratories, operated for the United States Department of Energy by Sandia Corporation.

Printed in the United States of America

Available from
National Technical Information Service
U. S. Department of Commerce
5285 Port Royal Road
Springfield, VA 22161

NTIS price codes
Printed copy: $8.00
Microfiche copy: A01

PAGES 1 to 2

WERE INTENTIONALLY

LEFT BLANK

SAND80-0454
Unlimited Release
Printed April 1981

GEOLOGIC FLOW CHARACTERIZATION USING TRACER TECHNIQUES

Robert D. Klett
Seabed Programs Division 4536

Craig E. Tyner
In Situ Technologies Division 4734

Sandia National Laboratories
Albuquerque, NM 87185

and

Eugene S. Hertel, Jr
The Dikewood Corporation
Albuquerque, NM

ABSTRACT

A new tracer flow-test system has been developed for in situ characterization of geologic formations. This report describes two sets of test equipment: one portable and one for testing in deep formations. Equations are derived for in situ detector calibration, raw data reduction, and flow logging. Data analysis techniques are presented for computing porosity and permeability in unconfined isotropic media, and porosity, permeability and fracture characteristics in media with confined or unconfined two-dimensional flow. The effects of tracer pulse spreading due to divergence, dispersion, and porous formations are also included.

ACKNOWLEDGMENTS

The authors wish to thank those who contributed to the development of the tracer flow test system.

Hardware Development:	C. D. Northam
	E. F. Richardson
	W. C. Riggan
	W. C. Wilson
Field Test Operation:	P. M. Drozda
	R. D. Jacobson

CONTENTS

TABLES

ILLUSTRATIONS

ILLUSTRATIONS (Cont)

GEOLOGIC FLOW CHARACTERIZATION USING TRACER TECHNIQUES

1. Introduction

The ability to measure fluid flow characteristics of geological formations is at least helpful and often essential for gas, oil, and water extraction, geothermal energy utilization, in situ coal gasification, in situ oil shale retorting, and nuclear waste isolation. These flow characteristics include formation transmissivity; locations and effective hydraulic radii of cracks; and location, thickness, porosity, and effective permeability of porous or rubbled layers. These properties cannot be measured in the laboratory because:

1. Crack patterns in rocks or packing of granular material are disturbed during sample acquisition,
2. Stresses are relieved when the samples are removed from the formation,
3. The formations are not homogeneous, and
4. Flow paths in geologic formations are not continuous.

This necessitates in situ measurements in the region and depth of interest.

Some measurements are made to characterize a formation and others are made to determine the effects of mechanical, thermal, or chemical alterations. An example of the latter is the explosive rubbling to facilitate flow in an oil shale retort where the extent of fracturing and the distribution of porosity, permeability, and surface area are of interest. In contrast, nuclear waste repositories require a tight formation with a high resistance to flow; in this case, loss of integrity due to thermal alteration is of interest. In both cases, flow tests are needed before and after the alterations to analyze the mechanisms.

Because of limited accessibility, highly variable and nonuniform formations, and, in some cases, the requirement of minimal disturbance of the formation, no one testing method can obtain all the data in all formations. In fact, many formations cannot be completely characterized using all of the test techniques that are available. In addition to the tracer flow test system described in this report, there are numerous other techniques that can be used to provide supplementary data:

1. Flow nets are used to map streamlines and equipotential lines for steady groundwater flow in confined or unconfined aquifers. The nets are constructed using potentiometric surfaces generated by measuring the water level in nonproducing wells. As few as three wells are needed to define groundwater flow at a specific location.[1-3] Direction of flow can be read directly from the flow nets. If permeability is known, the flow rate can be computed; if porosity is also known, velocities can be computed. Aquifers with anisotropic permeability can be handled using transforms.

2. Pump-down and recharge of wells can be used to obtain qualitative information such as communication between wells below given levels and relative water contents. Some quantitative data on groundwater flow and permeability can be obtained.[2,3] Natural groundwater movement is measured by putting a tracer in one well and measuring the time required for the tracer to reach wells in the downstream direction.

3. Geophysical methods can be used to help understand regional hydrology by measuring infiltration capacity, locating water tables, and defining the stratigraphy of the formation. Techniques[2,4] include magnetic, gravity, seismic, electrical resistivity, spontaneous electrical potential, core logs, caliper logs, radioactive logs, and infiltrometers. Acoustic techniques[5] have generally been ineffective in providing the detail necessary for formation evaluation. Surface uplift measurements can provide some information on void creation during fracturing events.[6] Downhole TV logging can yield information on visible fractures in the immediate vicinity of a wellbore.[6] The porosity of some formations can be determined by grouting or potting a well and then coring or overcoring the filled region.[7] Although the core will show the voids, it does not indicate if there is continuity for fluid flow. Flow channels between wells can be located by pumping a geologic dye between the wells prior to grouting to stain the walls of the open channels.

4. A downhole flow logging system measuring total gas flow versus depth will yield information on permeability of a formation as a function of depth,[8] although little information on the type of fracturing or rubbling responsible for the flow paths can be obtained with the system. Steady flow is established between two wells, and a flow-rate meter is placed in the bottom of the outlet well. The meter is slowly raised and a plot of flow rate versus depth is obtained. Uniform permeability is represented by a steady increase in flow rate. A step increase in the flow rate represents a horizontal crack and a ramp represents a vertical or angled crack. Quantitative data can be obtained using the pressure drop between holes and the rate of flow change with depth. Flow rates can be measured with hot-wire anemometers or turbine-type meters. The gas flow logger has some limitations: measurements cannot be made in low-permeability formations; the outlet well must have a uniform smooth cross section that can be sealed with wipers; and test wells must be fairly large, because the flow meters are in the logger.

5. Flow measurements between two wells (without tracer) can provide information on the overall transmissivity of a formation; however, little detail on the distribution of flow throughout the formation is obtained. Two-well tracer flow systems using injection and detection at the surface have provided some qualitative information on the number and type of flow paths in some formations.[9-11] Locations of the flow paths could not be measured and the output from different flow

paths could not be separated. Also, because the flow path through the wellbores can be long compared to that through the formation, the system can suffer from a serious loss of resolution in measurements of both tracer arrival time and pulse spreading. Another qualitative tracer-test system measures flow around a packer in a single drill hole.[12] Flow paths from a well to the surface can be found by pumping a gas tracer such as SF_6 into a well, capping all surrounding wells, and traversing the surface with a detector (sniffer).

The tracer flow system described in this report can be used in some formations and configurations to obtain quantitative data not possible with other test methods. Measurements are made between two or more drill holes, so disturbances to the formation made by drilling have a negligible effect on the test region. Since measurements are made using tracers and multiple downhole sensors, no well seals are required, and tests can be made in rubbled regions. These features, along with downhole injectors, make it possible to determine the location of two-dimensional flow paths and to separate data from multiple-flow paths. A three-dimensional flow version is also available for isotropic formations. Quantitative data, including porosity, permeability, and fracture sizes, can be obtained for many formations.

Section II of this report describes the total tracer flow system; Section III describes two types of test equipment for gas flow using Kr-85 tracers; and Sections IV and V contain the derivations for data reduction and analysis. Several options are given for both testing and data reduction. The options selected will depend on the formation examined and the data required.

II. Tracer Test System

The tracer test system measures flow properties between two or more drill holes. The major differences between this and similar systems is the additional downhole injection and sensing, and the associated methods of data reduction.[3,13,14] There are two basic test configurations; the systems for two-dimensional flow between parallel drill holes shown in Figure 1, and the system for three-dimensional flow between well ends shown in Figure 2. Both configurations can operate with either gas or liquid carrier fluids and either chemical or radioactive tracers and detectors. Air and water are the most common carrier fluids. In addition to being readily detectable, the tracer must be nondegradable, not absorbed by the formation, not masked by existing minerals, not ingested by organisms, and nonpolluting. Therefore, the selection of the tracer can be location- and formation dependent.

Krypton-85 is a typical radioactive gas tracer used with Geiger tube, semiconductor PIN, or scintillation detectors. Sulfur hexafluoride (SF_6) is a typical chemical gas tracer used with gas chromatograph detectors. Numerous tracers can be used in liquids, including methanol and ethyl alcohols, acetone, MEK, formic acid, acetic acid, formaldehyde, acetaldehyde, sugar, sodium,

potassium, lithium, phenols, iodine, EDTA, and nonbiodegradable detergents. Tracer detection is usually by chemical analysis, but in some cases electrical conductivity measurements can be used. Although gas flow tests are faster and usually more convenient than liquid tests, their applications are limited to situations where flow of gas is of interest or where the formation is dry or can be pumped dry. In the latter situation, the formation must be blown dry using pressures higher than the test pressure. Any capillary water remaining in the formation could result in erroneously low permeability measurements.

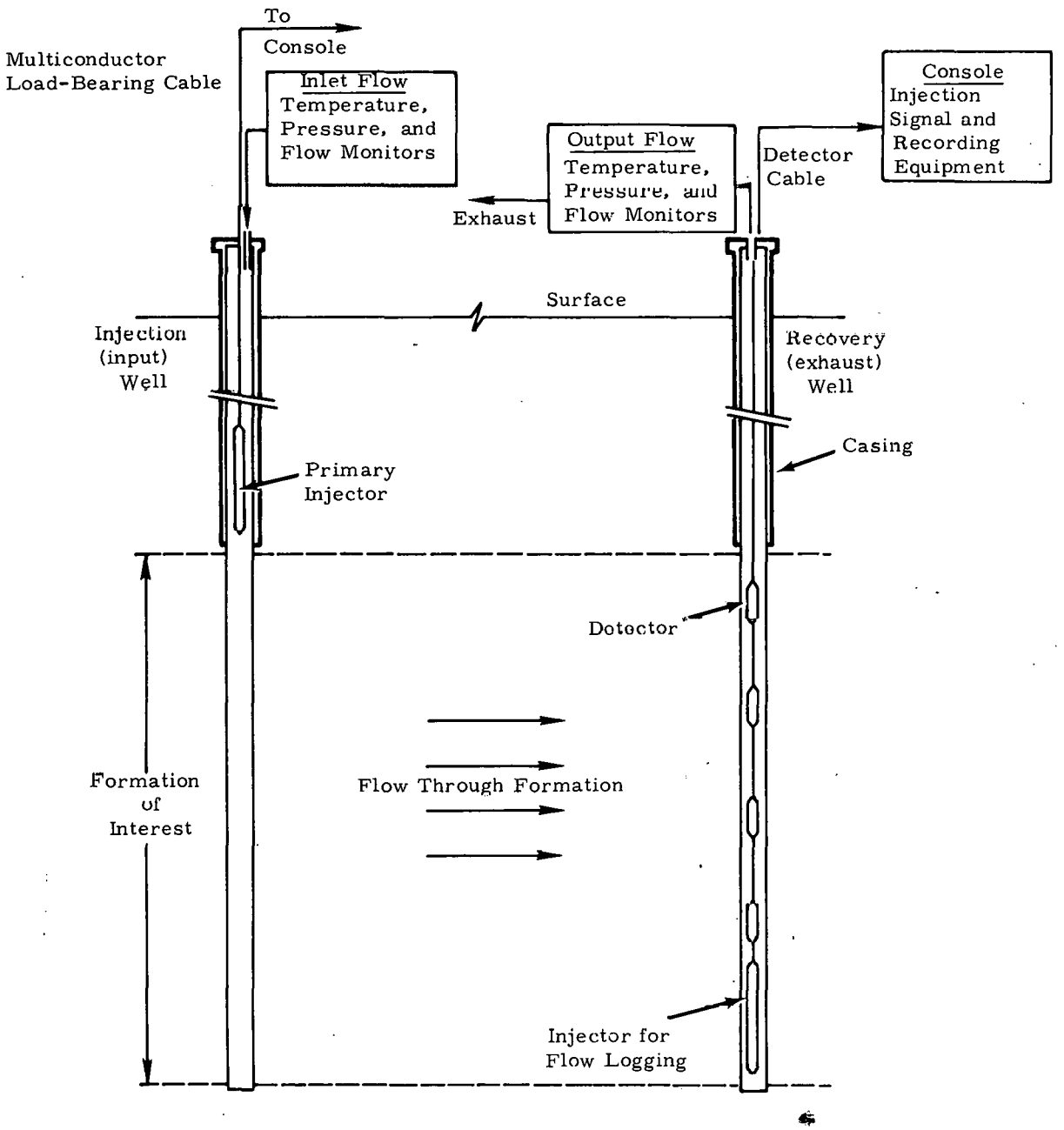

Figure 1. Tracer Flow System for Two-Dimensional Flow Between Wells

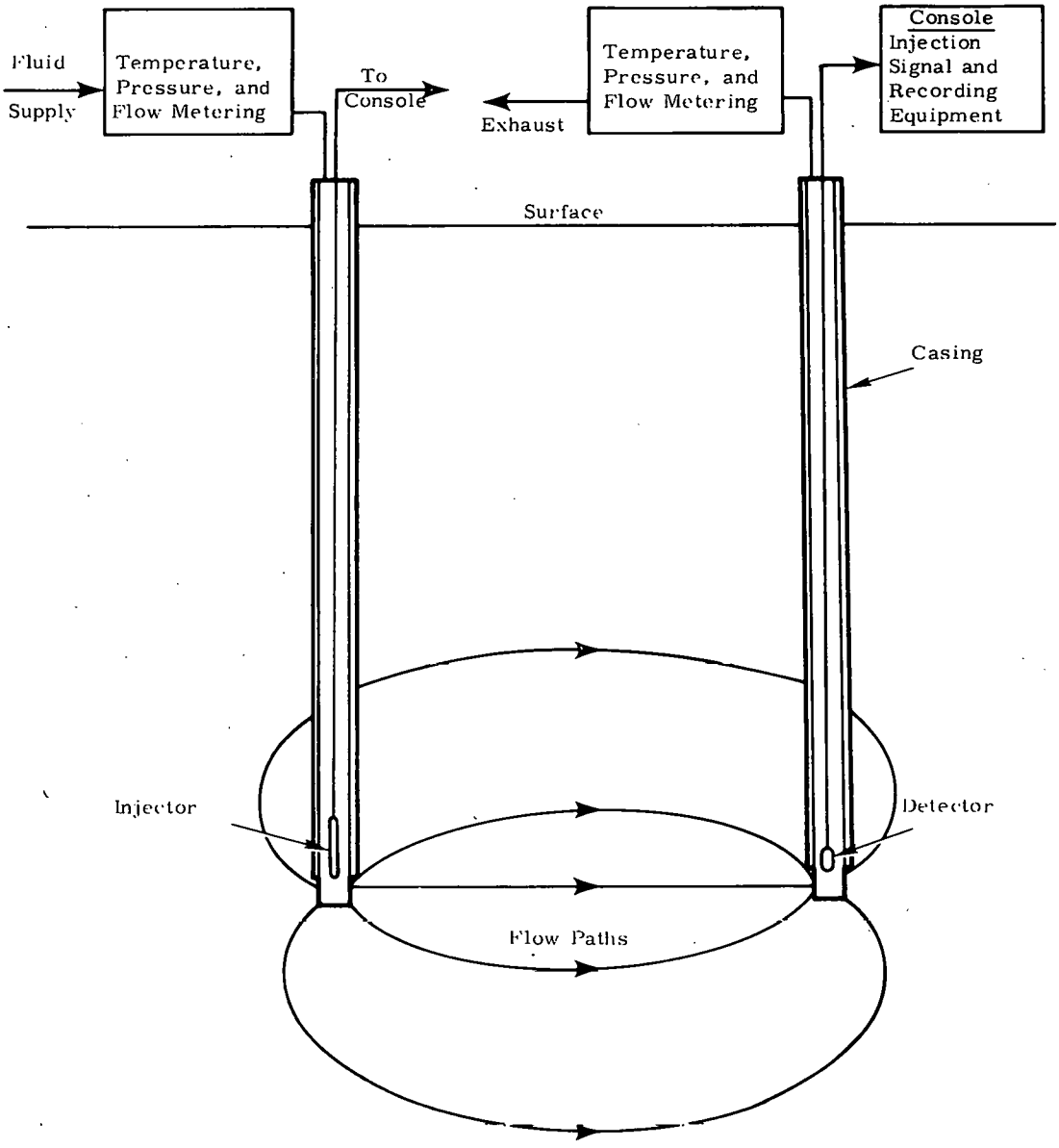

Figure 2. Tracer Flow System for Three-Dimensional Flow Between Well Ends

Temperatures, pressures, and flow rates at the inlet and outlet of the well can be measured either with an automated metering system or simpler manual flow panels. Tracer injectors are electronically controlled from the surface and are the positive displacement type, capable of multiple injections between refills. The output of the detectors is recorded on strip charts or magnetic tape.

In operation, the flow-metering equipment indicates when steady flow has been established between the wells. The next step for the two-dimensional flow system is calibration and flow logging. A short (usually < 1 s), rectangular pulse of tracer is released by the recovery well injector and

travels up the well and past the detector string. The tracer intensities versus time, as measured by the detectors, are used for flow logging (i.e., measuring location and magnitude of flow into the recovery well (Section IV)). These data are also needed to reduce the raw tracer data taken when the tracer is injected in the input well. While steady flow between the two wells is maintained, a short tracer pulse is injected into the input well at the top of the region of interest at the same time the detector recorders are started. The tracer travels to the exhaust well through various flow paths and the tracer intensity is measured as a function of time by the detector string. A pulse that is detected at a deep location is repeated as it passes each higher detector. The times of arrival of the tracer at the sensors, the area under the pulses, the pulse spreading, the decay rate of the pulses, and data from the flow logging test are used in conjunction with the flow rates, temperatures, and pressures measured by the flow metering equipment and well geometries to compute the flow properties between wells (Section IV). The tracer from the input well is also used for in situ calibration of the sensors by equating integrated detector outputs. In situ calibration is important because detector sensitivity varies with lateral position of the detector and flow patterns in the well (Section IV).

Flow logging in the exhaust well can be refined by adding more sensors or repeating the run with the sensors moved to different locations. Flow logging in the input well is done by:

- Reversing the test equipment,
- Adding a detector string in the input well (Figure 3 and Section IV), or
- Using packers in the input well (Figure 4), and making repeated tests with the injection region in different locations.

The flow system for three-dimensional flow requires only one injector and one detector because the wells are cased almost to the end of the hole (Figure 2). In situ calibration and raw data reduction are not required for the three-dimensional flow version. Therefore, a secondary injector in the exhaust well is not needed. Data analysis techniques are given in Section V. The selection of the two-or three-dimensional system depends on the formation to be tested. Neither system is limited to vertical drill holes.

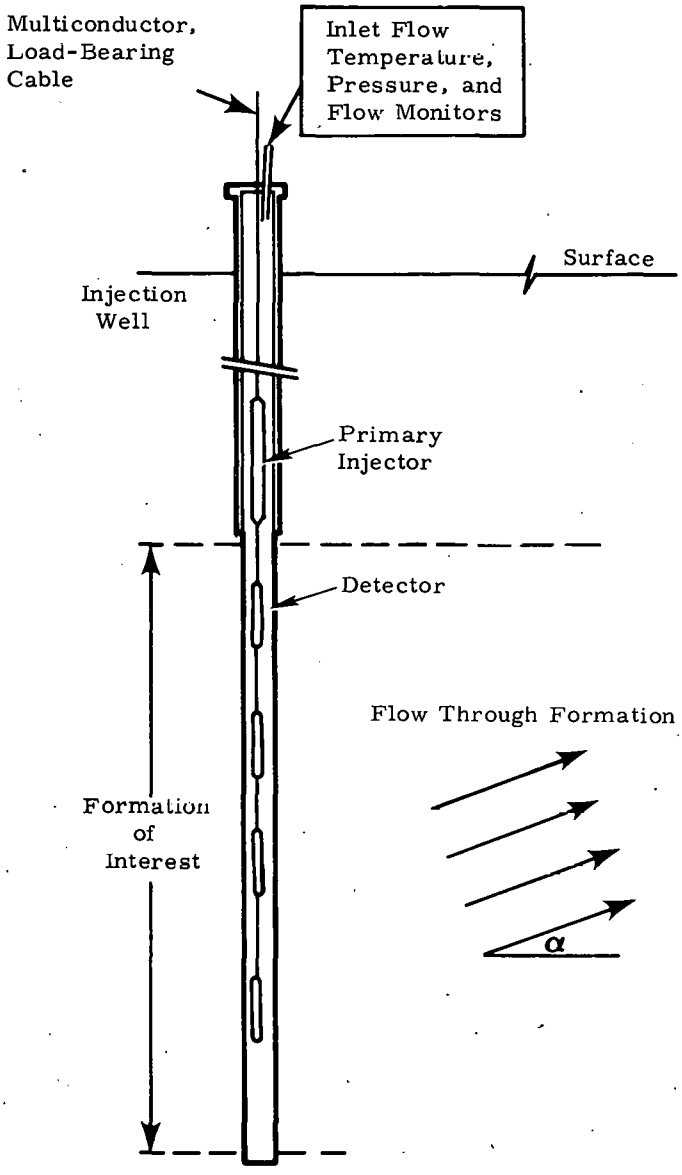

Figure 3. Optional Detectors in the Injection Well

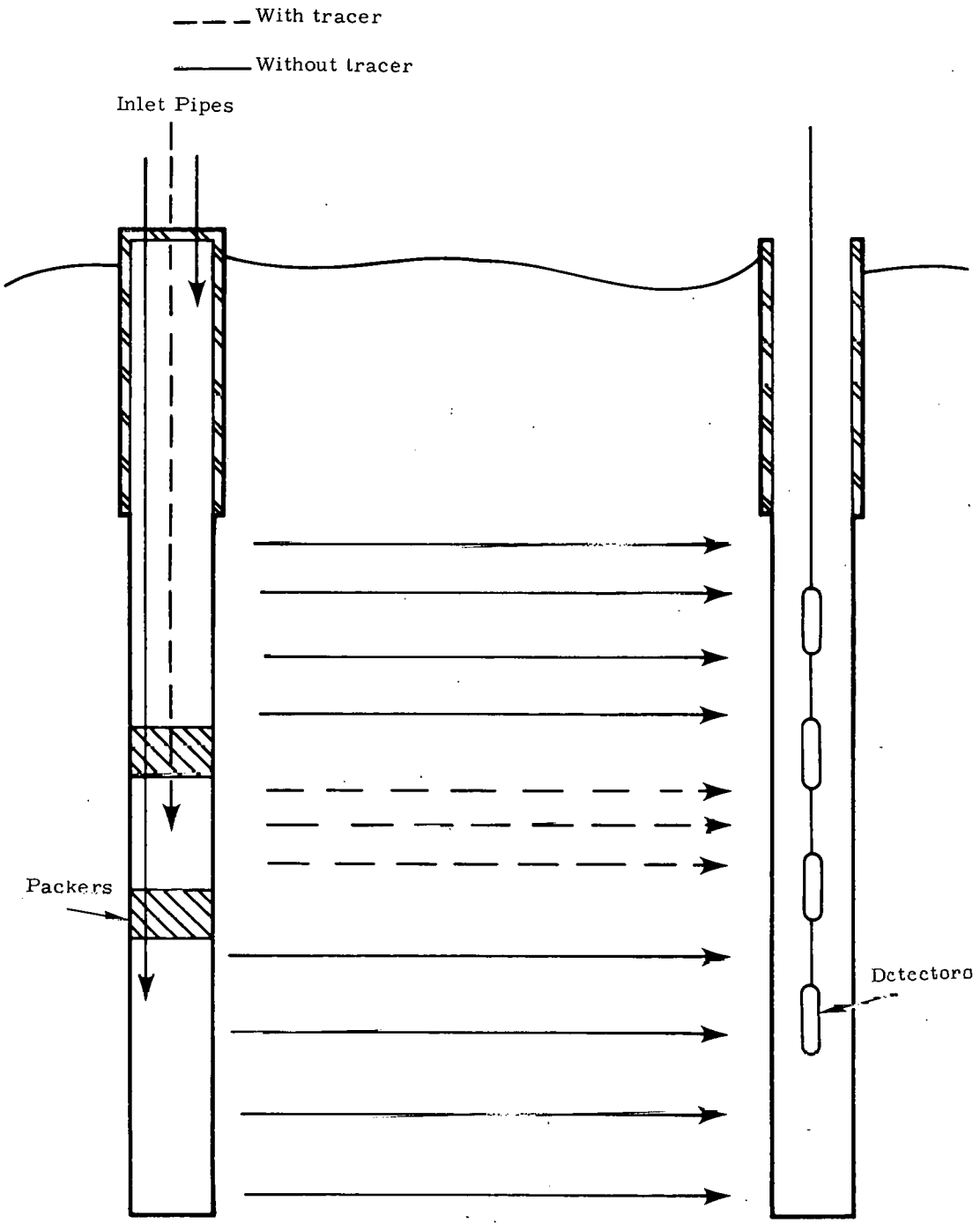

Figure 4. Optional Injection Between Packers Through Three Inlet Pipes, All at the Same Pressure

III. Test Equipment

There are two tracer flow systems currently in operation at Sandia National Laboratories. Both use air as the carrier, Krypton-85 as the tracer, and Geiger-Müller tubes as detectors. One system was designed primarily for testing in oil shale formations and is capable of operation at depths to 600 m. This system operates from a van that contains a powered draw works and automated control, recording, and data reduction equipment. The other system is smaller and lighter and was designed for testing to depths of 20 m in less accessible locations such as mine drifts. It is less expensive but requires hand emplacement of downhole equipment and manual data readout.

Automated Deep Well System

Figure 5 is an artist's conception of the deep well system, showing the field support van and instrumentation placement in a cutaway formation. This system consists of a downhole tracer injector located in an injection wellbore, and four downhole detectors plus a second injector in a production wellbore. (Figure 1 illustrates the system schematically.) Injector and detector systems are capable of operating at depths to 600 m (1970 ft) in 7.6-cm (3-in.) or larger diameter wellbores. Cabling systems are compatible with standard field equipment and procedures. The injector systems are capable of injecting (at pressures up to 6.9 MPa (1000 psi)) up to 60 pulses of the tracer gas on one filling. The detector system includes an array of four detectors with variable 0.6- to 5-m spacing between detectors. The gas flow metering system used with the tracer apparatus is capable of measuring flows between 0.3 and 170 m^3/hr. The details of each component of the system are discussed below.

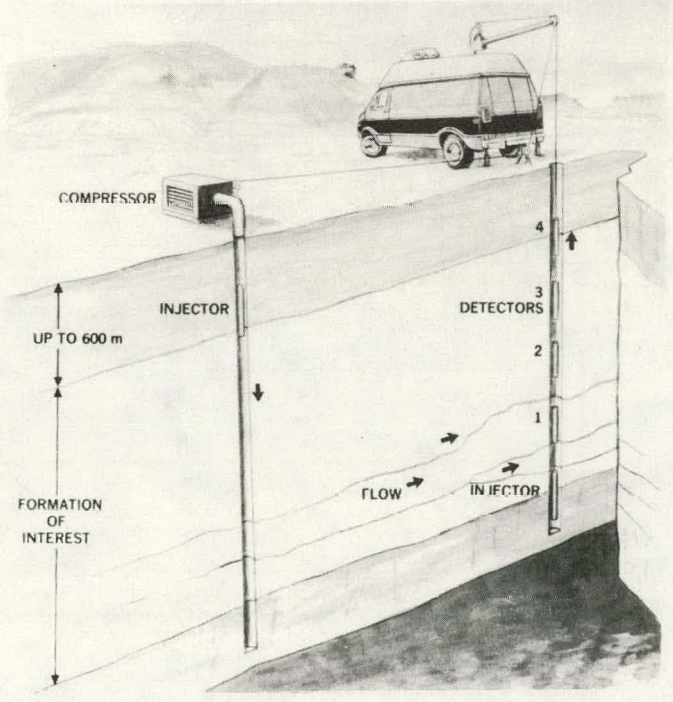

Figure 5. Artist's Conception of Deep-Well Tracer Flow Test System

The injector module (Figure 6) is a 1.5-m × 6.3-cm-diameter cylinder, with a 160-cm^3 bladder accumulator connected through a solenoid valve to the outlet. The remaining volume of the cylinder is pressurized and used to drive the accumulator. This volume can produce up to 60 approximately equal-sized pulses of tracer gas at 6.9 MPa (1000 psi), the maximum injection wellbore pressure for which the system is designed. The injector is suspended on approximately 600 m of seven-conductor cable. Low voltage (28 V) electrical pulses transmitted down one conductor of the cable are used to operate the solenoid, giving control from the surface of the amount of tracer injected. Additional control of injected tracer quantities can be achieved by careful dilution of the tracer prior to loading of the injector module.

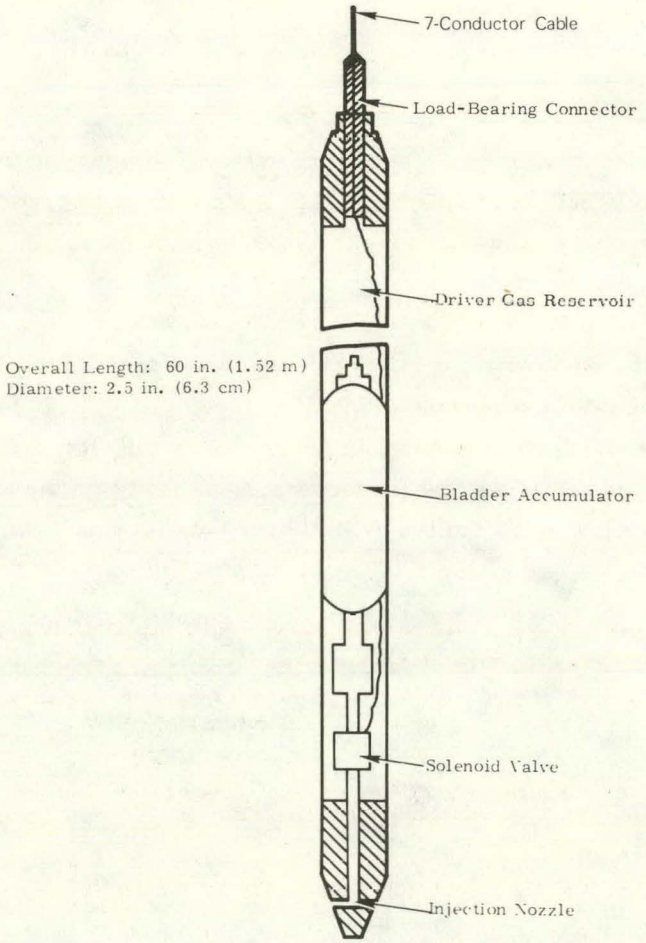

(a) Schematic

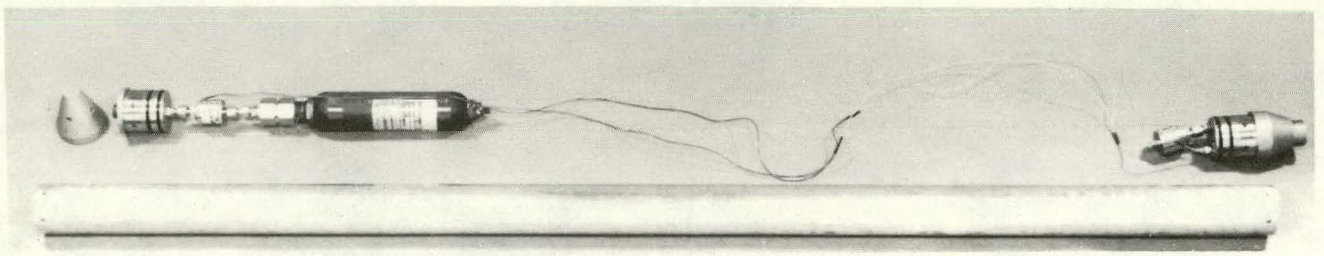

(b) Disassembled

Figure 6. Injector Module

The arrangement of the detectors in the recovery well is illustrated in Figure 1. An individual detector is shown both physically and schematically in Figure 7. The spacing between the four detectors used in the recovery well can be varied to provide the required resolution and formation coverage. The active element in each detector is a 25 cm long Geiger-Müller (GM) tube. To provide maximum sensitivity to Kr-85 decay (99.5% of which is beta), the tube is unshielded except for a flow-through protective case. Power is brought to each detector by one lead of a seven-conductor cable. The 28-Vdc signal is filtered and then stepped up to 900 to 1000 Vdc by a dc/dc converter to drive the GM tube. The detected signal (ac) is amplified and transmitted to the surface on the same line that supplies the dc power. All electrical components are waterproofed for use in wet environments.

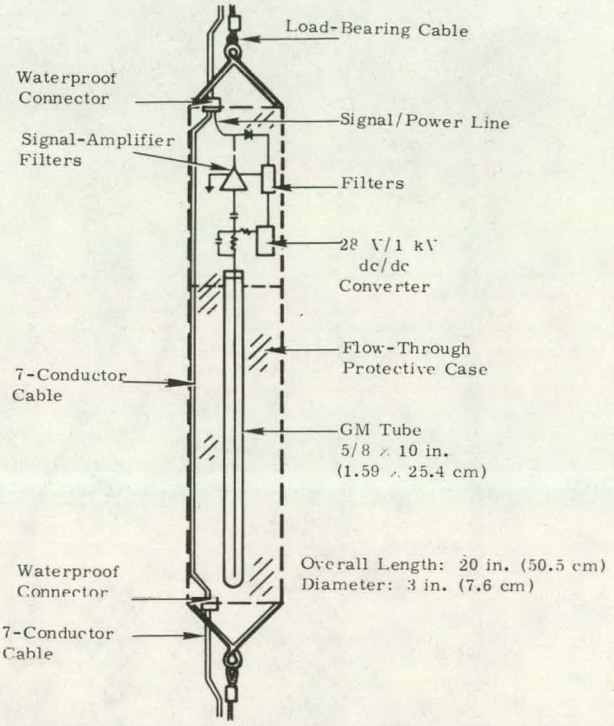

(a) Schematic

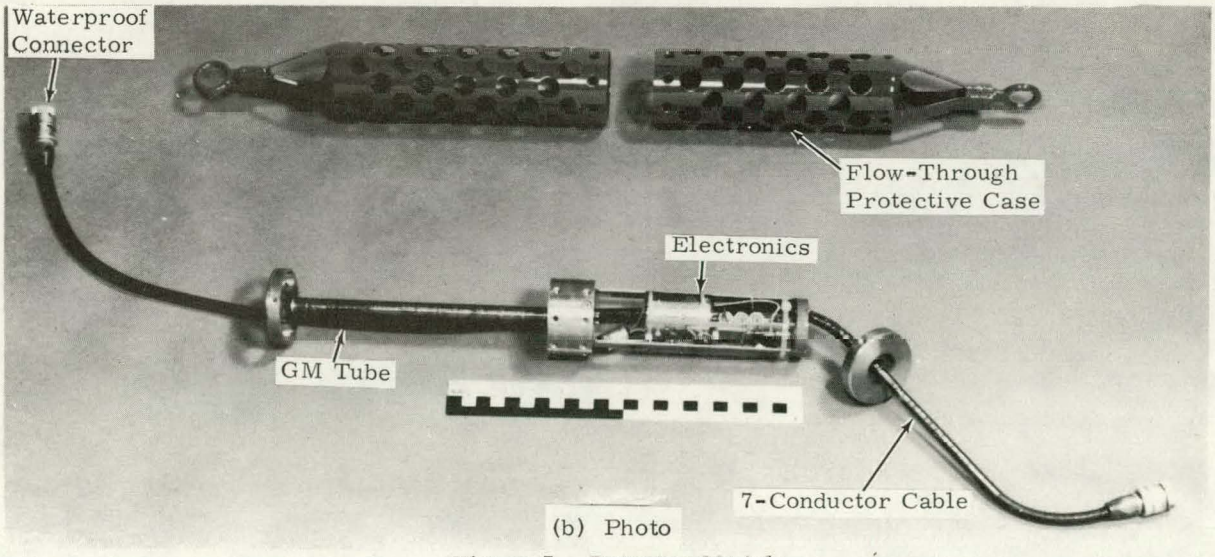

(b) Photo

Figure 7. Detector Module

A second injector (similar to that described above) is suspended below the bottom detector to provide tracer pulses of known size for the purpose of flow logging during tracer tests. This injector is operated by electrical signals sent over one of the remaining conductors of the main cable.

The seven-conductor nonload-bearing cable used between detectors terminates immediately above the top detector at a junction box. The junction box is connected to the surface by 600 m of standard load-bearing, seven-conductor cable. Equipment below the junction box is supported by 0.32 cm aircraft cable. Figure 8 shows all the downhole equipment for the option shown in Figure 1.

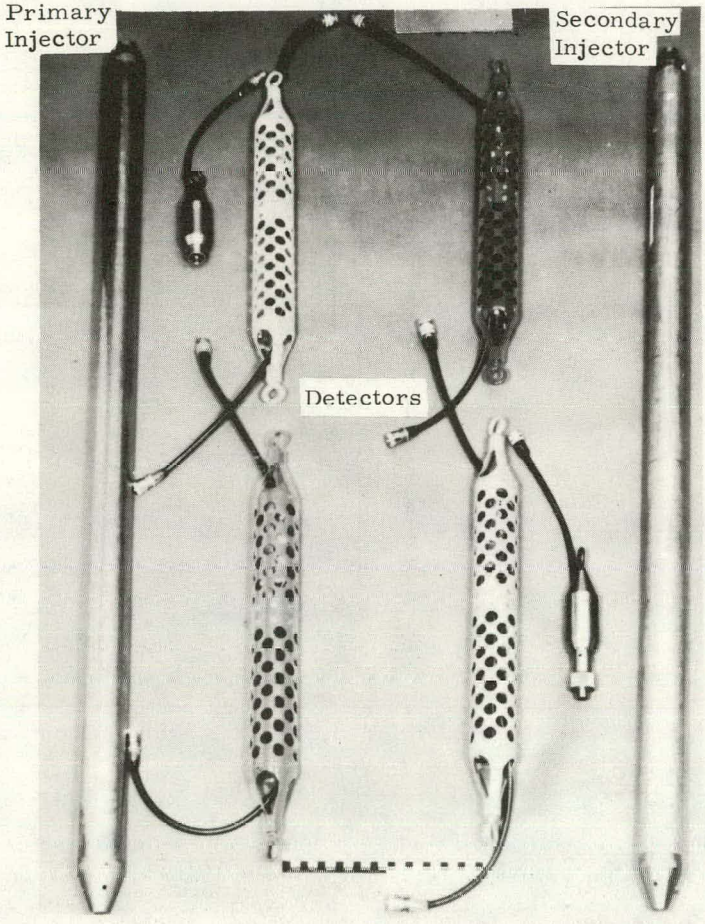

Figure 8. Downhole Equipment

Additional instrumentation to support the tracer tests includes a remote-reading flow meter measuring the total gas flow at the top of the recovery well. Recovery well temperature and pressure are also monitored at the surface (Figure 9).

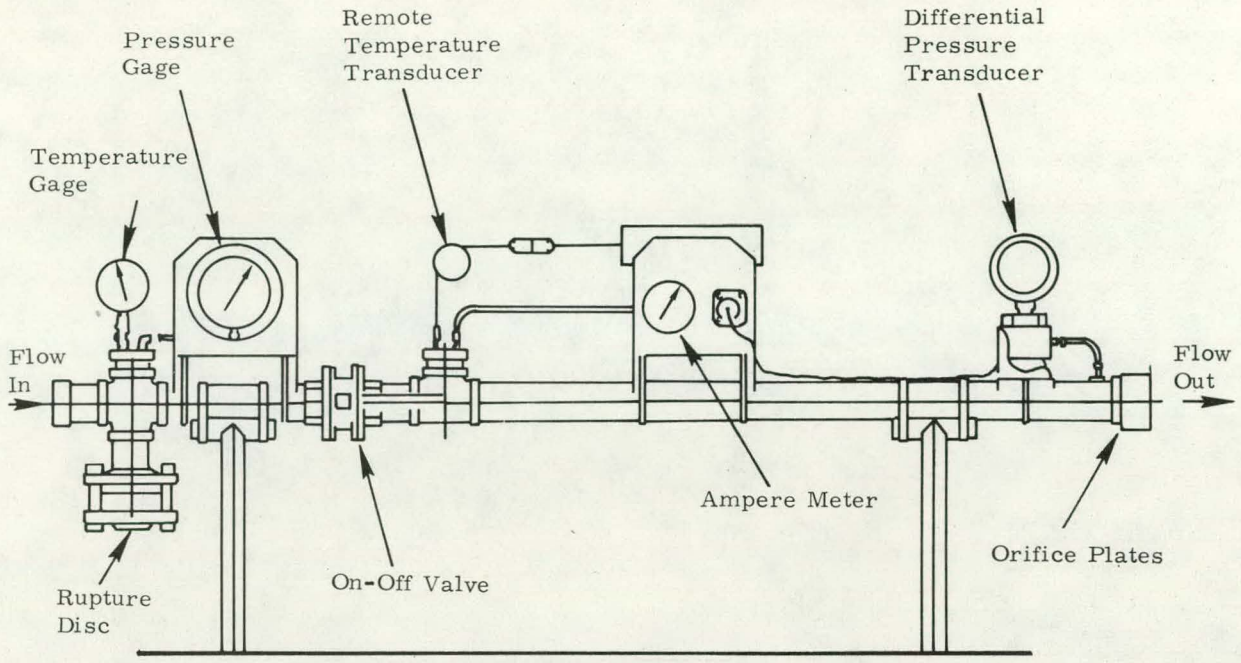

Figure 9. Typical Automated Flow Metering System

Control and data collection systems are contained in Sandia's Mobile Field Support Unit (MFSU), a self-contained four-wheel-drive van instrumented to support oil shale field experiments. Cabling and draw works for lowering the injector and detector systems downhole are also housed in the MFSU. Figure 10 shows the MFSU lowering the detector/injector string into the recovery well. This van is also used to operate the anemometer flow logger described in Reference 8.

The first step in the operation of a test is placing the injector in the injection well near the top of the formation of interest. Next, the detector string is lowered into the recovery well. Steady-state air flow is then established between the two wells. The logging injector attached below the detector string is fired at incremental depths in the region of expected flow paths, and the detector readings are noted. No detector response is an indication that the injector is below the bottom flow path in a stagnant region and the string must be raised before the test begins. The logging injector is also used to measure total gas flow versus depth in the recovery well. This is done by injecting a short pulse of tracer with this injector and monitoring the arrival time and intensity of the injected pulse as it travels up the wellbore past each of the detectors in turn. The primary injector is then fired for a known amount of time (typically 0.1 s), causing a pulse of tracer gas (typically 1 to 100 mCi) to be injected into the air flow. The pulse of tracer flows with the air through the formation to the recovery well. As the tracer enters the recovery well and flows up the wellbore, it is detected by the detector array.

Figure 10. Mobile Field Support Unit Emplacing Downhole Equipment in Recovery Well

Data from each of the detectors (i.e., GM tube outputs) are fed simultaneously into both digital and analog ratemeters. Analog ratemeter output is then recorded by a four-pen strip chart recorder for immediate operator observation. (Level detectors are used to start the chart recorder when a signal above background is first detected.)

The output of the digital ratemeters (i.e., counts per time interval in digital form for each channel) is recorded by a data logger at a selectable interval of 1 to 1000 s. Flow, temperature, and pressure data are also recorded by the data logger. In addition, when possible, the data are fed directly into a small minicomputer (housed in a separate trailer) for on-site data reduction. The tracer system has been field tested at several in situ oil shale retorts following a checkout under controlled conditions using a pipe network with flow restricted by valves and sand-packed sections of pipe.[13]

Portable Shallow Well System

The portable system operates in the same manner as the deep well system described in the previous section. The same detectors are used and the same injector can be used; a smaller model capable of about 10 pulses per filling is also available. For the three-dimensional flow option, only one injector and one detector are used as shown in Figure 2. Injectors and detectors are positioned by hand, and separate load-bearing and electrical cables are used. Flow is metered and regulated at the top of the injector and recovery wells using rotometers and temperature and pressure gauges mounted on the flow panels (Figure 11). A bypass is provided for startup. After flow is established, the flow rates are measured by one of the rotometers. The pressure regulator on the exhaust panel is used to provide the positive gauge pressure required in the recovery well for tests in some formations, such as:

a. Wet formations, in which the pressure in the test region must be maintained at or above the hydrostatic pressure to prevent water from returning after the formation has been dried.

b. Formations with very little resistance to flow, which require pressure in the recovery well to limit flow to reasonable rates.

c. Formations in which back pressure is needed to simulate a high-pressure process that could open flow passages.

Data is read manually, and the only data reduction that is done in the field is that which is necessary to verify test conditions and to assure that all the needed data is acquired.

When the walls of the recovery well are smooth and uniform, a mechanical flow logger can be used with the flow panels to provide supplementary data (Figure 12). This logger can be used in smaller diameter wells than other loggers[8, 15] because metering is done at the surface. However, it is limited to shallow depths. In operation, the wiper head (Figure 13) is lowered to the bottom of the recovery well and slowly raised to the surface while flow rates versus wiper depth are recorded. By changing the quick-disconnect low-pressure air line, the head can be converted from an integrating flow logger to an entry locator. Simultaneous entry locator and integrated flow readings can be made by using two output flow panels with hoses attached to each of the two outlets in the wiper head. Typical locator and integrated output traces are shown in Figure 12 for several types of flow paths.

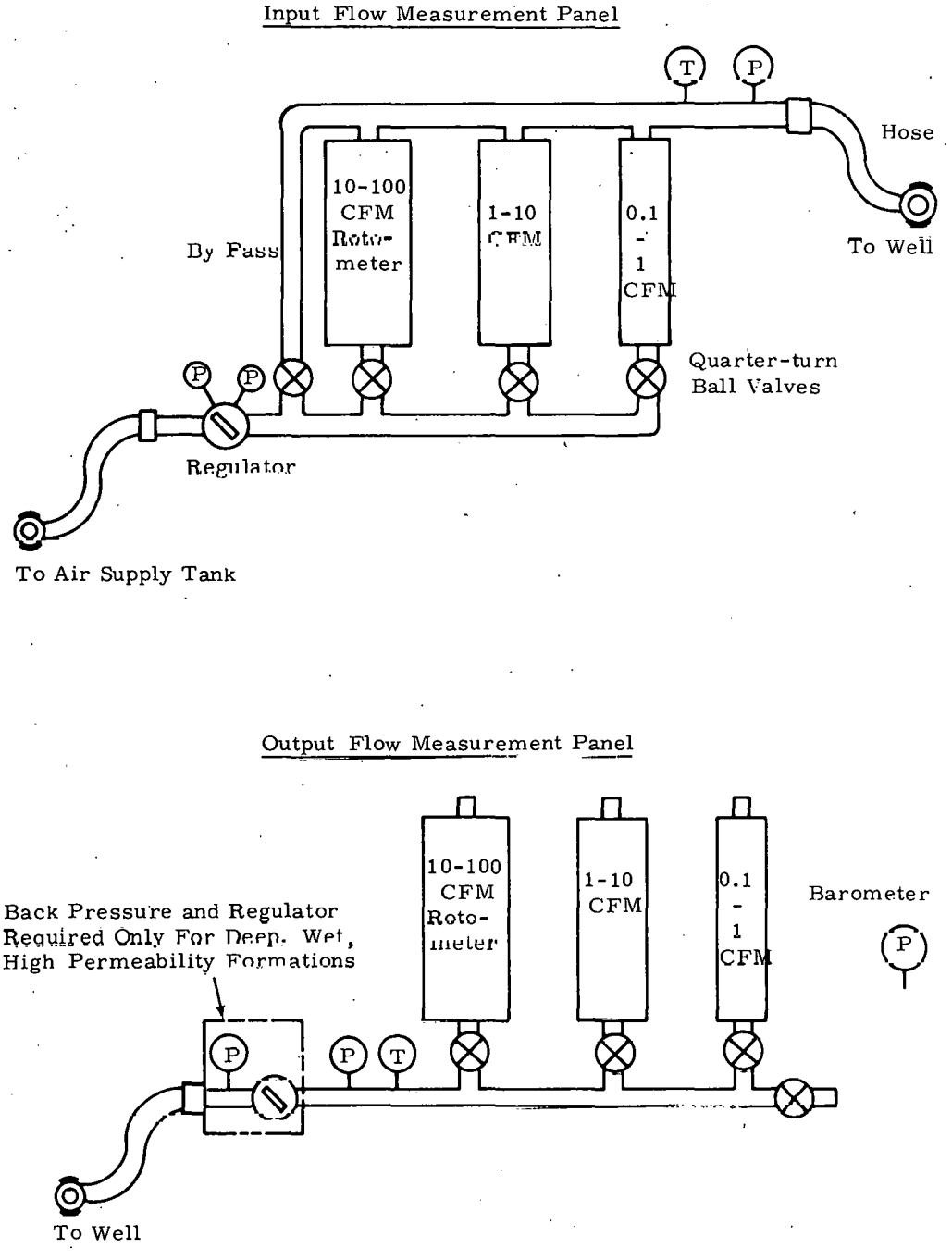

Figure 11. Portable Flow Metering System

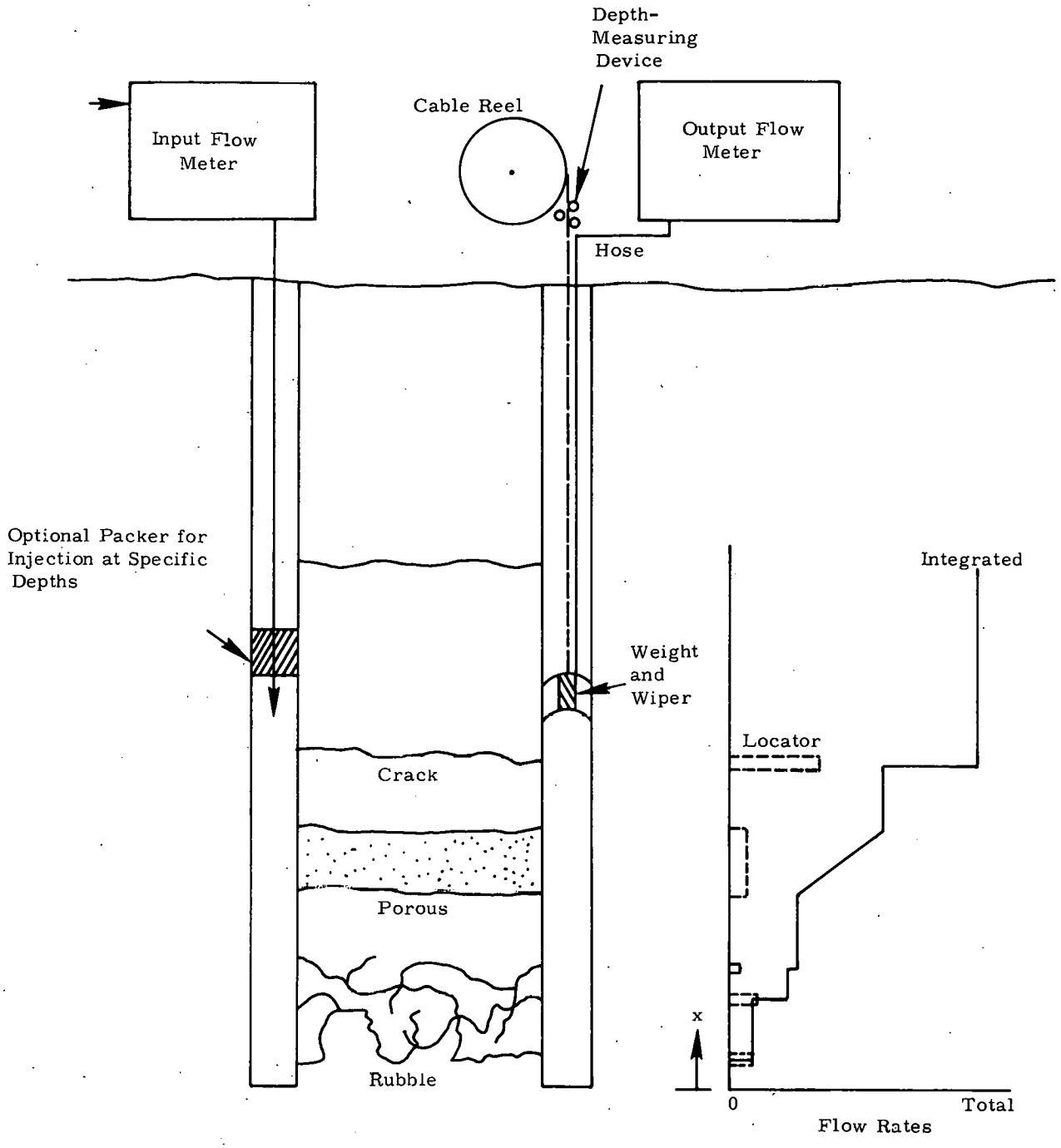

Figure 12. Flow Logger Attachment

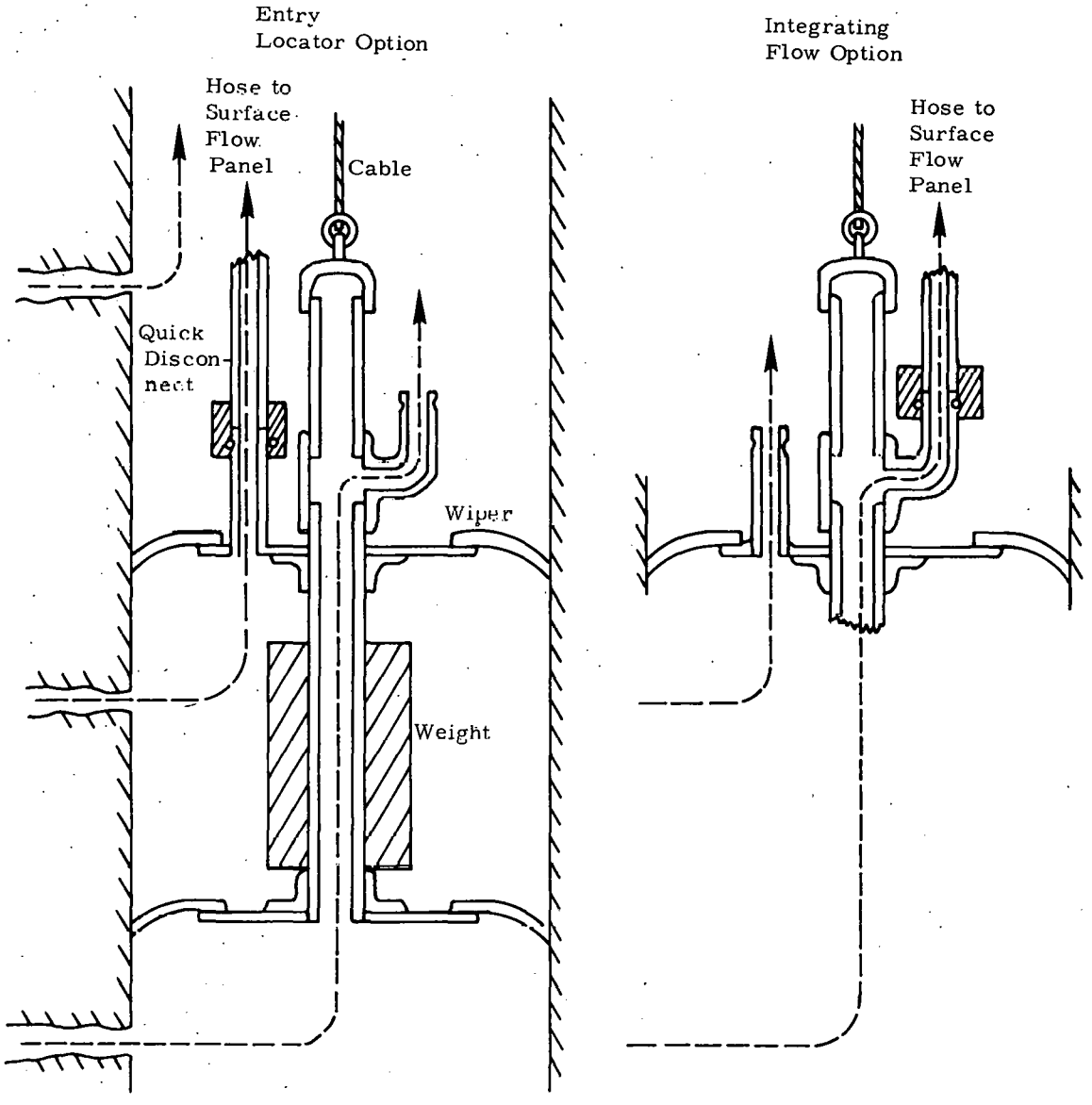

Figure 13. Wiper Head for Flow Logger Attachment

The other option that has been used with the portable system is the detector string in the injection well similar to that shown in Figure 3. This allows simultaneous logging of both wells.

The portable unit has been field-tested during near-surface heater experiments at Oak Ridge, Tennessee and the Nevada Test Site.

IV. Data Reduction and Analysis for Two-Dimensional Flow

The data reduction and analysis techniques derived in this section are for two-dimensional flow perpendicular to the injection and recovery wells (i.e., in the x,y plane). The test configurations used to obtain the input data for these techniques are those shown in Figures 1 and 3. Porous, rubbled, and fractured formations are covered. Analyses are applicable to test regions confined only by planes perpendicular to the wellbores or completely enclosed by impermeable boundaries. Included are in situ calibration, raw data reduction, corrections for compressible flow, computations for porosity, permeability and fracture size, and the effects of streamline divergence, dispersion along stream lines, and porous region pulse spreading. Although the air/Kr-85/GM tube system is used for illustrative purposes, these data reduction techniques can be adapted to any tracer/carrier-fluid/detector system.

In Situ Calibration

In situ calibration of the GM tubes is important because sensitivity varies with lateral position of the detector in the well, flow constrictions caused by the detectors and cables, and flow patterns in the well. This calibration can be accomplished in the injector well because, as part of the carrier fluid and tracer flow into the formation from the well, the amount of tracer in the injection well is reduced by the same ratio by which the velocity is decreased. As a result, there is no change in the number of detected tracer decays at any point in the well. The amplitude and duration of the GM tube output pulse remains the same; the only change in pulse shape is caused by boundary-layer spreading as the tracer flows down the well. Therefore, the sensitivity of all injection well sensors can be adjusted to give the same reading from a pulse released from the primary injector.

Similar principles apply to recovery well calibration. The single pulse in the injection well becomes multiple pulses in the recovery well caused by flow through different paths in the formations. The pulses are also spread out by divergence and dispersion. Therefore, the integrated output of the recovery well detectors, rather than the output amplitudes, must be equated for calibration. Only the primary injector can be used for calibration since detector output from a flow-logging injector pulse becomes smaller as flow enters the recovery well from the formation. (When the primary injector is used, flow entering the recovery well contains a fixed proportion of tracer.) Calibration in the recovery well is automatically accounted for in the raw data reduction technique developed in this report.

Tracer Flow Logging and Raw Data Reduction

In addition to characterization of the formation, the tracer tests can also be used for flow logging (i.e., measuring locations and quantities of fluids that enter or leave the wells for a given pressure differential). Except for certain situations that will be described later in this section, the locations of flow paths can only be defined as being between a pair of sensors. Changes in velocities in the wells, and hence in the times for a pulse to travel between sensors, are proportional to quantity of fluid that has entered or left the well. This principle can be used to compute

sizes of the flow paths between sensors in both wells. In the injection well, transit time between detectors is inversely proportional to the flow velocity in the well. In the recovery well, the reduction in the integrated signal (from the flow logging injector) between detectors is proportional to the flow entering between the detectors. The flow logging injector is used so that only one pulse passes the detectors and pulse separation is not needed. Logging of both wells can be helpful in determining the slope of flow paths, the branching of fractures, and fluid leakage from the test region.

No raw tracer test data reduction is required for the injection well, because only one pulse passes each detector, and the detector output does not change in amplitude or length as flow leaves the well. However, except in homogenous porous formations or those with very widely spaced fractures, the raw tracer data from the recovery well cannot be used in data analyses or for logging. The recovery well data reduction converts the raw data to the amount of tracer entering the well in the region below each tracer by separating the pulses and by correcting the amplitude of the pulse to account for dilution as flow enters the well. Recovery well data reduction includes the calibration, gives the result of the logging, and computes the amount of tracer entering the well in each region, all in one operation.

Injection-Well Logging*

In the injection well, the only detectable change in the tracer pulse as flow leaves the well is the change in velocity of the pulse. Using the equipment shown in Figure 3, the average velocity ($\bar{V}$) between two detectors is measured, using the time (Δt) for pulse travel from one detector to the next (Figure 14).

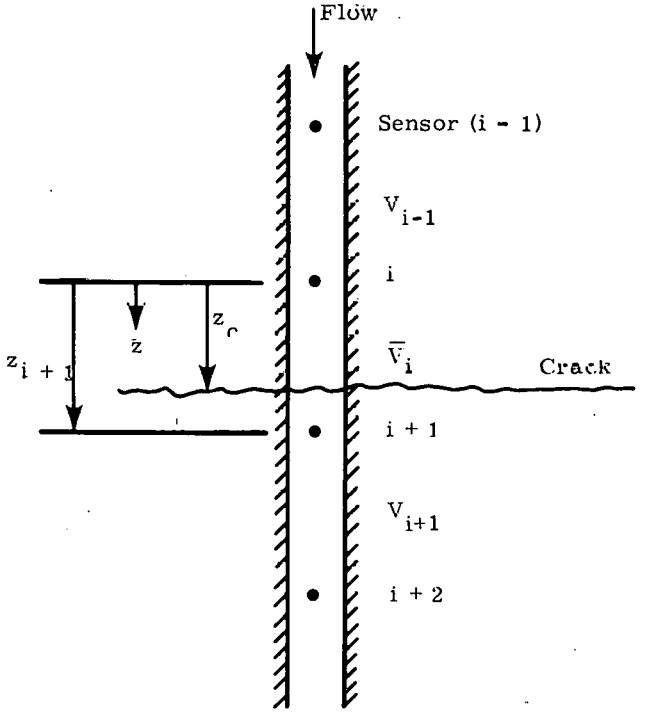

Figure 14
Injection Well Tracer Flow Logging

*Mathematical terms are defined in the Nomenclature section.

The average velocity is Δz divided by Δt, and the volumetric flow rate (Q) in the well is equal to the velocity times the unobstructed cross-section area of the well. With time data from only two sensors, neither the location of the flow path (z_c) between the sensors nor the flow into the crack could be computed, because a small crack near the top of Δz would have the same Δt as a large crack near the bottom of Δz. Therefore, sensor pairs with no flow losses above and below the fractured region (Figure 14) are needed to provide the needed input data. With this extra data, the flow into the crack can be computed, using

$$Q_c = Q_{i-1}\left(1 - \frac{V_{i-1}}{V_{i+1}}\right) , \tag{1}$$

and the location of the crack between the sensors is

$$z_c = z_{i+1}\left(\frac{\bar{V}_i - V_{i+1}}{V_{i-1} - V_{i+1}}\right) . \tag{2}$$

The requirement for a sensor pair between fractures limits this technique to formations with at least a meter between fractures.

The top pair of sensors can also be used as an input flow meter, using input pressure and temperature. Likewise, the top pair in the recovery well can be used as the output flow meter. In deep wells, there will be some boundary layer spreading in the injection well. The sensors in the vicinity of the flow paths define the shape of the pulse entering the formation, so the pulse spreading effects of the formation can be separated from those of the well.

Recovery Well Logging and Data Reduction

The tracer data collected by the data-acquisition system consists basically of the number of radioactive decays detected by each of the detectors as a function of time. To be of use in characterizing the formation, these data must be converted to the amount of tracer entering each of the regions of the wellbore (associated with a detector) as a function of time. The raw data reduction and flow logging steps are described in detail below.

Figure 15 shows schematically the wellbore, the detector string, and the division of the wellbore into n regions, one below each detector. Region i is that region between detectors i and i-1, where i = 1 is defined as the bottom detector (Region 1 is all that below detector 1). Q_i is the total steady state volumetric flow rate past detector i, and q_i is the steady state flow into Region i of the wellbore. Q_i is simply the sum of the q_i's for all regions below the i^{th} detector.

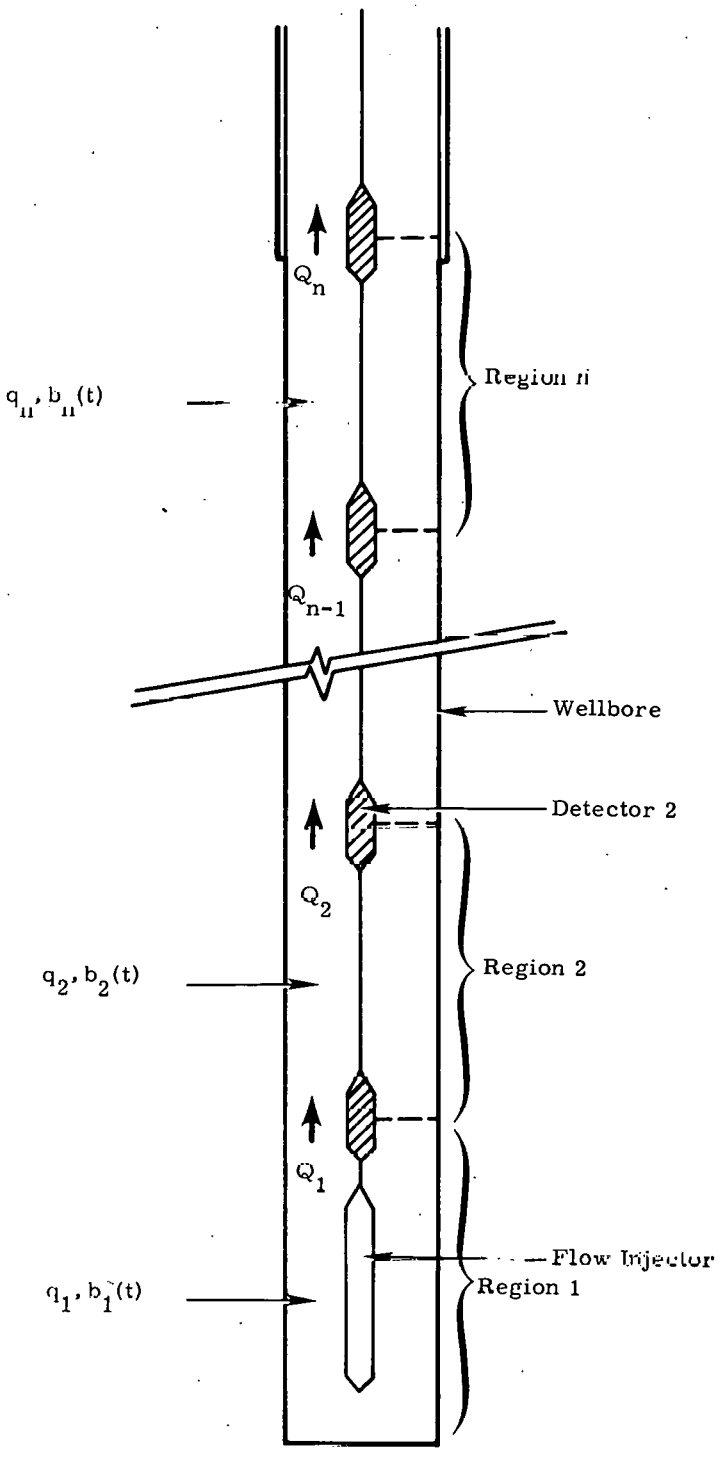

Figure 15. Recovery Well Geometry

During the tracer test, B_T curies of tracer (Kr-85) are released nearly instantaneously in the injection wellbore. The tracer is assumed to mix radially with the carrier gas (air) immediately (a good assumption, given the geometry of the injection nozzle). The tracer then travels through the formation (with the carrier), with $B_i(t)$ ci/s passing detector i. The $B_i(t)$'s are related to the actual quantities of interest, $b_i(t)$ (the number of tracer ci/s arriving in Region i), by the relationships

$$b_1(t) = B_1(t) \tag{3a}$$

$$b_i(t) = B_i(t) - B_{i-1}(t - \ell_i) \ , \quad i = 2 \ \text{to} \ n \tag{3b}$$

where ℓ_i is the time required for flow in the wellbore from detector i-1 to i. The ℓ_i's may be determined directly from tracer flow test data (the times between pulse arrival at each of the detectors) or, if the ℓ_i's are very small (as they frequently are), more easily from the approximate relationship

$$\ell_i \approx \frac{A_i' \, d_i}{(Q_i + Q_{i-1})/2} \tag{4}$$

where d_i is the distance between detectors i and i-1, and A_i' is the average cross-sectional area available for flow between those same detectors. ($A_i' = (v_i - v_i')/d_i$ where v_i is the volume of wellbore and v_i' the total volume of the hardware between detectors i and i-1.)

Consider a single atom of tracer passing detector i. The probability that a decay from that atom will be detected by that detector can be given as

$$P_i = c_t c_i' \theta_i \tag{5}$$

where θ_i is the total time the atom remains in the vicinity of detector i, c_t is the probability per unit time that the atom will decay (a function of the tracer gas only), and c_i' is the probability that, if the atom decays while in the vicinity of the detector, it will be detected (a function only of the effective detector sensitivity; i.e., its inherent sensitivity coupled with its geometric cross section and position in the wellbore). θ_i can be expressed as

$$\theta_i = \frac{A_i'' \, \ell_i}{Q_i} \tag{6}$$

where ℓ_i is the effective length of the i^{th} detector element and A_i'' is the cross section available for flow at the detector.

The actual detected count rate at detector i, $N_i'(t)$, can then be given by

$$N_i'(t) = P_i B_i(t) + NB_i \tag{7}$$

$$= \frac{c_t c_i' A_i'' \ell_i}{Q_i} B_i(t) + NB_i \tag{8}$$

or

$$B_i(t) = Q_i c_i N_i(t) \tag{9}$$

where NB_i is the background count rate at detector i, determined from pretest conditions; c_i is defined as $c_i \equiv (c_t c_i' A_i'' \ell_i)^{-1}$; and $N_i(t)$ is the count rate above background ($N_i(t) = N_i'(t) - NB_i$). Note that this calibration factor c_i is a function of the tracer, the wellbore geometry, and the detector sensitivity, but not a function of the formation characteristics or the flow.

Substitution into Eq (3) then gives

$$b_1(t) = Q_1 c_1 N_1(t) \tag{10a}$$

$$b_i(t) = Q_i c_i N_i(t) - Q_{i-1} c_{i-1} N_{i-1}(t - \ell_i) \quad , \quad i = 3 \text{ to } n \; . \tag{10b}$$

Because tracer atoms travel through the formation with the carrier gas, the ratio of the time-integrated amount of tracer passing detector i to the flow past that detector must be the same as the ratio of total tracer injected to total flow injected (i.e., a constant). That is,

$$\frac{B_{iT}}{Q_i} = \frac{B_T}{Q_{inj}} = \text{Constant} \tag{11}$$

Or, substituting from Eq (9),*

$$c_i N_{iT} = \text{Constant for all i} \tag{12}$$

*The time-integrated value of any time-dependent function X(t) is defined as $X_T = \int_0^\infty X(t)\, dt$.

from which the more useful expression

$$\frac{c_i}{c_{i-1}} = \frac{N_{i-1\,T}}{N_{iT}} \quad \text{for} \quad i = 2 \quad \text{to} \quad n \tag{13}$$

can be obtained directly.

Solution of Eq (10) requires data from a tracer flow test, where a pulse of tracer gas B_{fT} is released from the flow injector at the bottom of the detector string in the production well. Proceeding in a manner analogous to the above analyses and labeling with a subscript "f" for flow test, the total amount of tracer entering the bottom region is

$$b_{f1\,T} = B_{fT} = Q_1 c_1 N_{f1T} \tag{14}$$

while for all other regions,

$$b_{fi\,T} = 0, \quad i = 2 \text{ to } n \ , \tag{15}$$

since tracer enters the wellbore only in the first (lowest) region during a flow test. The time-integrated form of Eq (10b) still applies. Therefore,

$$b_{fi\,T} = 0 = Q_i c_i N_{fi\,T} - c_{i-1} Q_{i-1} N_{fi-1\,T}, \quad i = 2 \quad \text{to} \quad n \tag{16}$$

or

$$Q_i c_i N_{fi\,T} = Q_{i-1} c_{i-1} N_{fi-1\,T} \equiv \text{Constant} \tag{17}$$

But this expression must hold for i = 2 (i - 1 = 1), and thus the constant must be equal to B_{fT} from Eq (14); i.e.,

$$Q_i c_i N_{fi\,T} = B_{fT} \quad \text{for all} \quad i \ . \tag{18}$$

The use of Eqs (13) and (17) allows the explicit calculation of the flow values Q_i (since Q_n is known by measurement at the surface); i.e.,

$$Q_{i-1} = Q_i \frac{N_{i-1\,T}}{N_{i\,T}} \frac{N_{fi\,T}}{N_{fi-1\,T}} \ , \quad i = n \quad \text{to} \quad 2 \tag{19}$$

Equation (19), which includes the calibration factor, can be used to log the recovery well; i.e., measure the volumetric flow rate past each detector.

Since the N_i's are known from the experiment and Q_n is known from a surface flow measurement, the remaining Q_i's can be determined. Table 1 shows the results of several flow tests at a calibrated test facility, giving both the known flows (from rotometer measurements) and flow test results. Agreement is excellent--an important result, since these values are necessary for complete analysis of tracer-test results as well as for flow logging.

Table 1

Experimental Flow Test Results

Detector	Known Flow (m^3/h)	Flow-Test Result (m^3/h)
4	15.86	15.86
3	15.86	15.96
2	15.86	16.01
1	15.86	16.09
4	17.56	17.56
3	17.56	17.12
2	9.06	9.90
1	9.06	8.90
4	16.42	16.42
3	16.42	16.84
2	12.18	12.80
1	12.18	13.35

Finally, substitution of Eq (18) into Eq (10) yields an explicit expression for the required quantities; i.e., the amount of tracer entering any region of the wellbore as a function of time:

$$b_1(t) = \bar{B}_{f\,T}\,\frac{N_{1(t)}}{N_{f1\,T}}\ , \tag{20a}$$

$$b_i(t) = B_{f\,T}\left[\frac{N_{i(t)}}{N_{fi\,T}} - \frac{N_{i-1\,(t\,-\,t_i)}}{N_{fi-1\,T}}\right], \quad i = 2 \quad \text{to} \quad n\ . \tag{20b}$$

Equations (20a) and (20b) are used to reduce the data to a form that can be used in data analysis to characterize the formation. A more detailed derivation of the data reduction and the computer program based on these equations can be found in Reference 16.

The calculational sequence used for flow logging $[Q_i]$ and data reduction $[b_i(t)]$ is summarized in Table 2.

Table 2

Calculational Sequence for Tracer Data Reduction

Known experimental data: $N_i(t)$, $N_{fi}(t)$, Q_n, B_{fT}

1. From $N_i(t)$ and $N_{fi}(t)$, calculate N_{iT} and N_{fiT}.
2. Calculate Q_i's sequentially from n - 1 to 1 from Eq (19)
3. Calculate ℓ_i's from Eq (4) (or use experimental peak arrival times from flow test if ℓ_i's are large relative to data interval).
4. Calculate $b_i(t)$'s from Eq (20).

Figure 16 illustrates the use of this calculational sequence in the reduction of a typical set of field data. The data are from a 1979 tracer test in an explosively fractured Antrim oil-shale formation at the Dow Chemical Company's true in situ field test site at Peck, Michigan. Formation depth was nearly 400 m. Figure 16a shows the raw tracer data (i.e., the four sets of normalized $N_i(t)$ curves versus time). Flow up of the wellbore of tracer entering Regions 1 and 2 is evident. Figure 16b shows the result of the data reduction scheme--the set of normalized $b_i(t)$ curves versus time. These data now show the actual locations and quantities of tracer flow (and hence total flow) into the wellbore.

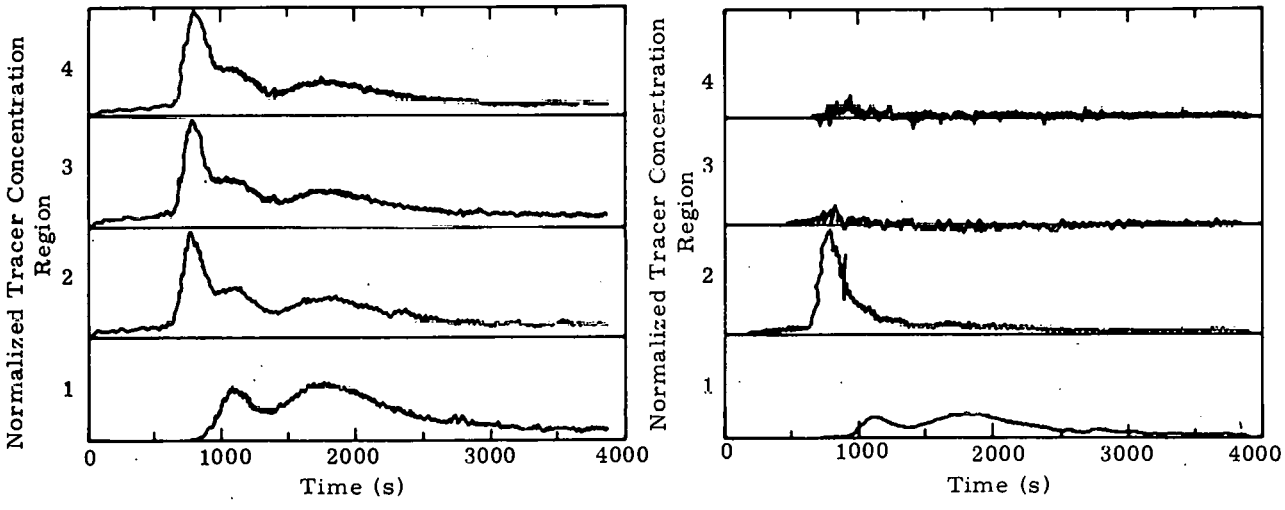

Figure 16. Sample Tracer Data

Data Analysis for Unconfined Flow

The type of flow considered in this section is confined by two impermeable boundaries perpendicular to the wellbores but unconfined in the radial direction. Streamlines and equipotential lines in a plane perpendicular to the wells are shown in Figure 17. The region can be porous, rubbled, or have fractures running perpendicular to the wells. This would be representative of natural or large altered formations.

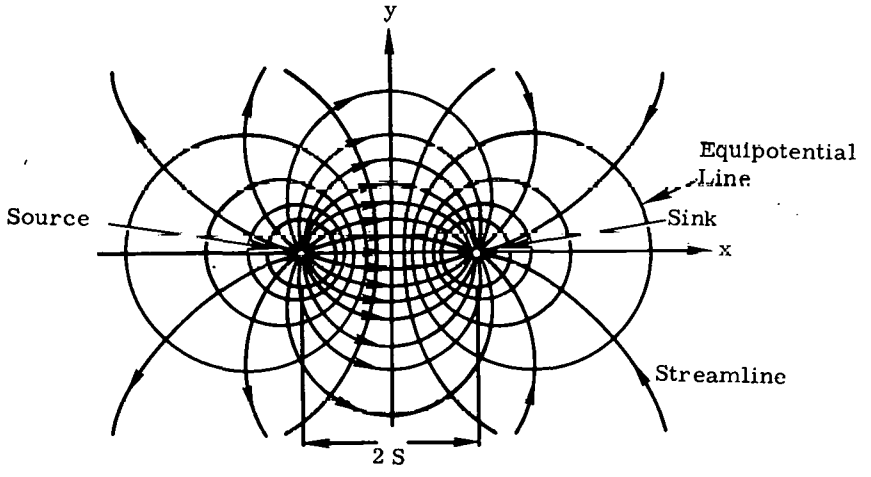

Figure 17. Equipotential and Streamlines for Flow Between Two Wells

The basic theory for two-dimensional flow between wells was developed in Reference 17. Using those results and the reduced data from the tracer tests, analytical techniques were derived to compute fracture sizes and frictional resistance in laminar and turbulent flow, the permeability and porosity of porous media, and the active void volume of flow paths. Temperatures, pressures, flow rates, and fluid properties used in these analyses are the mean values for the region being analyzed (i.e., injection well, formation, or recovery well). As an example, the flow rates given in the test output are typically expressed at standard pressure and temperature (P_o = 1 atmos, $T_o = 0^oC$). For use in data analyses, the standard flow rates must be multiplied by the factor $(P_o T_m / P_m T_o)$ where the subscript m denotes mean values for the region being analyzed.

Divergence of Streamlines-- The formation characterization equations derived in this section are based on stream and potential functions and the principle of superposition. The reduced test data used in the analyses include volumetric flow rate, temperatures, pressure, well spacing, well diameter, and the time of first arrival of the tracer pulse (t_F) at the detectors after it has traveled through the diverging/converging stream tubes shown in Figure 17.

Beginning with the complex potential for a line sink

$$\zeta = \frac{q}{2\pi}\left(\ell n\ r + i\ \theta\right) \qquad (21)$$

and using the principal of superposition and conversion to Cartesian coordinates, the velocity potential for a combined line source and sink is

$$\Phi = \frac{q}{4\pi} \ell n \left[\frac{(x - S)^2 + y^2}{(x + S)^2 + y^2} \right] \tag{22}$$

where S is half the distance between the source and sink. Equipotential lines are defined as constant values of $4\pi\Phi/q$ or

$$\frac{(x - S)^2 + y^2}{(x + S)^2 + y^2} = \text{a constant } C_1 \quad . \tag{23}$$

Equation (23) can be expressed as

$$\left(x - \frac{1 + C_1}{1 - C_1} S \right)^2 + y^2 = \frac{4 C_1 S^2}{(1 - C_1)^2} \quad , \tag{24}$$

which is the equation for a family of Apolonious circles with

$$r = \frac{2 S \sqrt{C_1}}{1 - C_1} \tag{25}$$

and centers at

$$x = \frac{S(1 + C_1)}{1 - C_1} \quad , \quad y = 0 \quad . \tag{26}$$

Using superposition, the stream function is

$$\Psi = \frac{q}{2\pi} \left(\tan^{-1} \frac{y}{x - S} - \tan^{-1} \frac{y}{x + S} \right) \quad . \tag{27}$$

Streamlines are defined as constant values of $2\pi\Psi/q$, so the streamline equation is

$$x^2 + \left(y + \frac{S}{C_2} \right)^2 = S^2 \left(1 + \frac{1}{(C_2)^2} \right) \tag{28}$$

which is a family of circles with

$$r = S \sqrt{1 + (C_2)^{-2}} \tag{29}$$

and centers at

$$x = 0,\ y = \frac{S}{C_2} \quad . \tag{30}$$

Equations (24), (25), (26), (28), (29), and (30) define the flow paths and potentials in Figure 17.

The x component of velocity (V_x) is the only part of the velocity vector that is needed to compute flow times between the wells. V_x can be found using

$$V_x = -\frac{d\Phi}{dx} = -\frac{d\Psi}{dy} \quad . \tag{31}$$

Differentiating either Eq (22) or (27), yields

$$V_x = \frac{q}{2\pi}\left[\frac{(x+S)}{(x+S)^2 + y^2} - \frac{(x-S)}{(x-S)^2 + y^2}\right] \tag{32}$$

Equation (32) gives the apparent velocity based on q. If the flow is through a porous medium, the actual velocity is obtained by dividing Eq (32) by the effective porosity (ϵ). Void volumes in the effective porosity exclude isolated voids and stagnant regions.

Along the shortest path ($y = 0$) between wells in a porous formation, the actual velocity would be

$$\left(V_x\right)_{y=0} = \frac{q}{\pi\epsilon}\left(\frac{S}{S^2 - x^2}\right) \quad . \tag{33}$$

The variation in velocity with x is caused by the divergence of streamlines.

Since the well radius $a \ll S$ for most applications, V_x at $x = -(S - a)$ is almost the same as $-V_x$ at $x = -(S + a)$. Therefore, the flow is nearly uniform in all directions from the well walls. From Eq (33), the time of first arrival of a tracer in the sink well after it is introduced in the source well is

$$t_F = \frac{2\pi\epsilon}{qS}\int_0^{S-a}\left(S^2 - x^2\right)dx \quad . \tag{34}$$

After integration,

$$t_F = \frac{2\pi S^2\epsilon}{q}\left[\frac{2}{3} - \left(\frac{a}{S}\right)^2 + \frac{1}{3}\left(\frac{a}{S}\right)^3\right] \quad . \tag{35}$$

From the potential equation for a line source and sink (22) and from the hydraulic conductivity definition

$$\Phi = K\frac{P}{\rho g} + \text{Constant} \quad , \tag{36}$$

the equation for the pressure drop between the wells can be written

$$\Delta P = \frac{q\rho g}{2\pi K} \ln\left[\frac{(2S - a)^2}{a^2}\right] \quad . \tag{37}$$

Using the output from Eq (19),

$$q = \frac{Q_i - Q_{i-1}}{\Delta z} \quad , \tag{38}$$

provided both detectors are in the permeable region. Δz is the distance between detectors. Using Eq (35) and q from Eq (38), the porosity for $a \ll S$ is

$$\epsilon \approx \frac{3t_F q}{4\pi S^2} \quad . \tag{39}$$

With q known, Eq (37) can be used to compute the hydraulic conductivity.

$$K \approx \frac{q\bar{\rho}g}{\pi(\Delta P)} \ln\left(\frac{2S}{a}\right) \tag{40}$$

where $\bar{\rho}$ is the average density of the carrier fluid between the wells.

Alternatively, if the porosity can be estimated and q cannot be measured, the hydraulic conductivity can be found using t_F instead of q. Combining Eqs (35) and (37),

$$K = \frac{\rho g S^2 \epsilon}{(\Delta P)t_F}\left[\frac{2}{3} - \left(\frac{a}{S}\right)^2 + \frac{1}{3}\left(\frac{a}{S}\right)^3\right] \ln\left[\frac{(2S - a)^2}{a^2}\right] \tag{41a}$$

for $a \ll S$

$$K \approx \frac{4\rho g S^2 \epsilon}{3(\Delta P)t_F} \ln\left(\frac{2S}{a}\right) \quad . \tag{41b}$$

Also, if porosity can be estimated, the combined thickness of thin porous layers between two detectors can be found by rearranging Eq (39).

$$\sum h_i = \frac{3\, t_F \left(Q_i - Q_{i-1}\right)}{4\pi\epsilon S^2} \quad . \tag{42}$$

Analysis of flow through fractures begins with

$$\frac{dP}{dr} = \frac{fV^2\rho}{2R_H} \tag{43}$$

where

$$V = \frac{q}{2\pi r} \qquad \text{and}$$

$$R_H = \frac{h}{2} \qquad \text{for a fracture.}$$

For laminar flow in a fracture,

$$f_L = \frac{8\mu}{hV\rho} \quad . \tag{44}$$

Making the substitutions into Eq (43) and integrating,

$$P_2 - P_1 = \frac{4\mu q}{\pi h^2} \ln\left(\frac{r_2}{r_1}\right) \quad . \tag{45}$$

Using superposition, the pressure difference between the wells is

$$\Delta P = \frac{8\mu q}{\pi h^2} \ln\left[\frac{(2S - a)^2}{a^2}\right] \quad , \tag{46}$$

which is analogous to Eq (36) for porous flow.

Combining Eqs (35) and (46), and eliminating the porosity term, the fracture thickness when $a \ll S$ is

$$h_L \approx \left[\frac{32\, S^2 \mu}{3\, t_F (\Delta P)} \ln\left(\frac{2S}{a}\right)\right]^{\frac{1}{2}} \quad . \tag{47}$$

The analysis for turbulent flow is similar to that for laminar flow, except that the substitution for the friction factor (Eq (44)) cannot be made. If an estimate of the friction factor can be made, the fracture thickness with turbulent flow is

$$h_T \approx \frac{8 f S^2 \rho}{3 t_F^2 (\Delta P)} \ln\left(\frac{2S}{a}\right) . \tag{48}$$

The alternative is to compute the frictional resistance of the fracture ($N = fL/R_H$).

$$N_T = \frac{4 fS}{h} \approx \frac{3 t_F^2 (\Delta P)}{2 S^2 \rho \ln\left(\frac{2S}{a}\right)} . \tag{49}$$

Tracer flow test data can be used to characterize porous formations using Eqs (40) and (41) and fractures using Eqs (47), (48), or (49).

Although equivalent pipe diameters do not help characterize the formation, they can be useful for sizing hardware for subsequent operations (such as retorting) between the wells. Using flow test data, flow resistance between wells would be equivalent to that of pipes of the following diameters:

$$DE = \left[\frac{256 \mu \bar{Q} S}{\pi (\Delta P)}\right]^{0.25} \tag{50}$$

for laminar flow and

$$DE = \left[\frac{64 f \bar{Q}^2 \rho S}{\pi^2 (\Delta P)}\right]^{0.2} \tag{51}$$

for turbulent flow.

Pulse Decay Characteristics in the Recovery Well -- Transit times for streamlines other than along the shortest path (t_F) are also used to characterize the formation. The relative concentration [C(t)] of a tracer in the recovery well depends on the initial pulse and the streamtubes through the formation. Reference 18 contains a derivation of the relationship which expresses the transit time as a function of streamline angle. That relationship is

$$\begin{aligned} t(\alpha) &= t_F \qquad \alpha = 0, 2\pi \\ t(\alpha) &= 3 t_F \frac{1 - \alpha \cot \alpha}{\sin^2 \alpha} \qquad 0 < \alpha < 2\pi \end{aligned} \tag{52}$$

where $\alpha = \beta_2 - \beta_1 - \pi$ and t_F is the time of first arrival for a negligible well radius. β_2 and β_1 are defined in Figure 18.

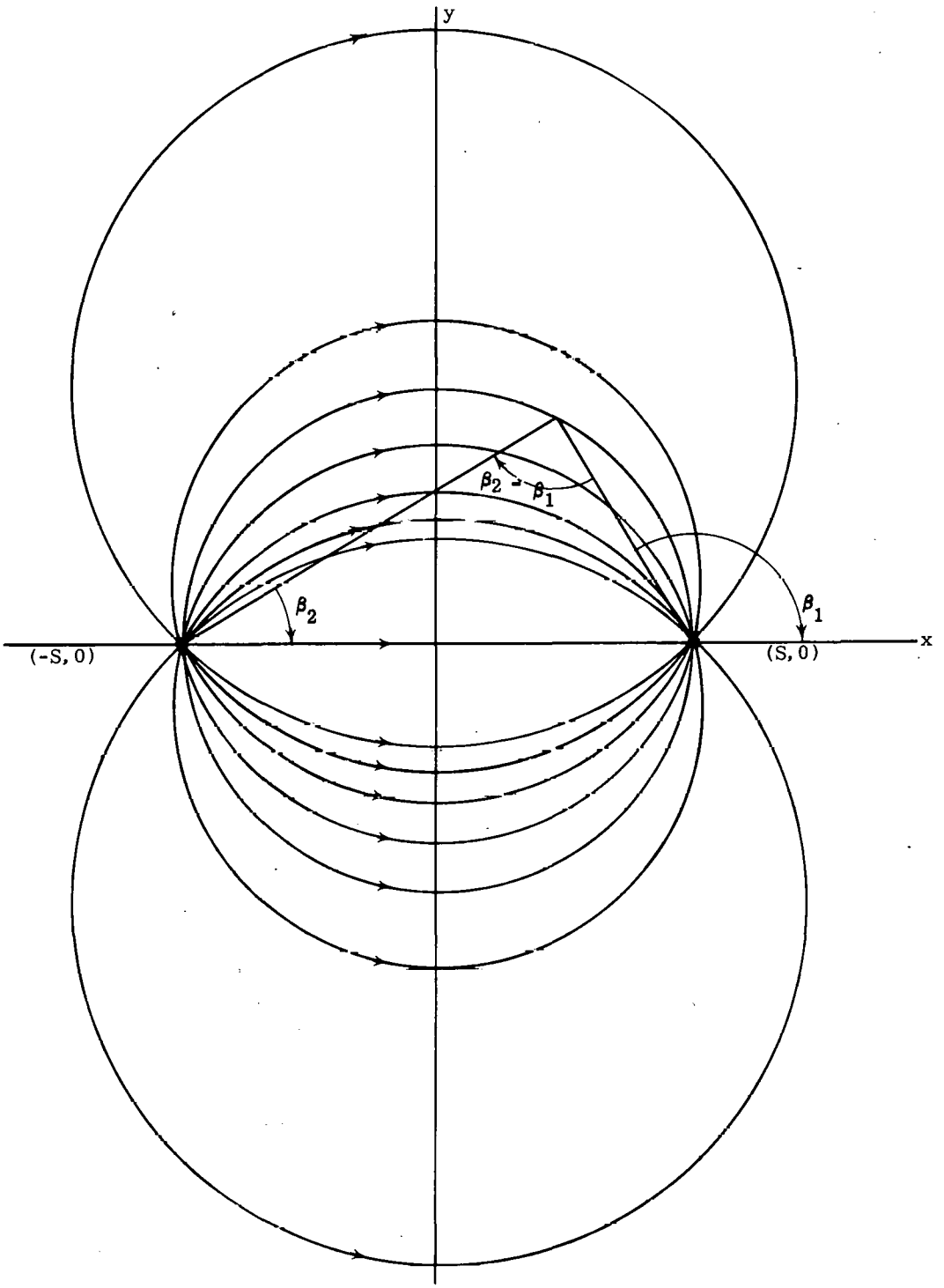

Figure 18. Streamline Layout and Definition of Streamline Angle α for an Infinite Line Source and Sink ($\alpha = \beta_2 - \beta_1 - \pi$)

If the tracer is introduced at the source well as a step function change in concentration, the temporal distribution of the tracer will not be a step function, since the travel time is different for each streamline. The relative concentration of tracer in the output well at any time t is the average concentration over all the streamlines arriving at that time; the relative concentration of tracer in the output well is given by

$$C(t) = \frac{2\,\xi(t)}{2\pi} = \frac{\xi(t)}{\pi} \quad , \tag{53}$$

where $\xi(t)$ is the streamline (represented by α) having transit time equal to t. It is not possible to invert Eq (52) and express the function ξ directly. However, the relative (normalized) concentration can be plotted versus time. This is done in Figure 19. As a function of τ, which is the ratio of time to t_F, the relative concentration is approximately

$$\begin{aligned} C(\tau) &= 0 && \tau < 1 \\ C(\tau) &= 1 - \exp\left[-\lambda(\tau - 1)\right] && \tau \geq 1 \quad . \end{aligned} \tag{54}$$

Since the current test equipment uses a narrow rectangular pulse or delta function input, no further analysis was conducted on the continuous step input pulse.

The time dependence of a tracer for a delta function can be determined from step-function information[19] by taking the slope of the curve in Figure 19(a). The relative concentration of tracer in the recovery well shows the effects of streamline divergence in Figure 19(b) as a function of τ; Figure 19(b) is of the form

$$\begin{aligned} C(\tau) &= 0 && \tau < 1 \\ C(\tau) &= C_o \exp\left[-\lambda(\tau - 1)\right] && \tau \geq 1 \quad . \end{aligned} \tag{55}$$

This function was least-squares fitted to the data in Figure 19(b). The decay constant (λ) was found to be 1.16. In terms of real time, Eq (55) becomes

$$\begin{aligned} C(t) &= 0 && t < t_F \\ C(t) &= \exp\left[-1.16\,(t - t_F)\right] && t \geq t_F \quad . \end{aligned} \tag{56}$$

A measurement of the decay constant from experimental results would allow a determination of t_F.

Measurement of the full width at half maximum or the decay constant from analysis of the test data would allow two additional methods of calculating t_F. These measurements would use

$$t_F = 1.16/\lambda \tag{57}$$

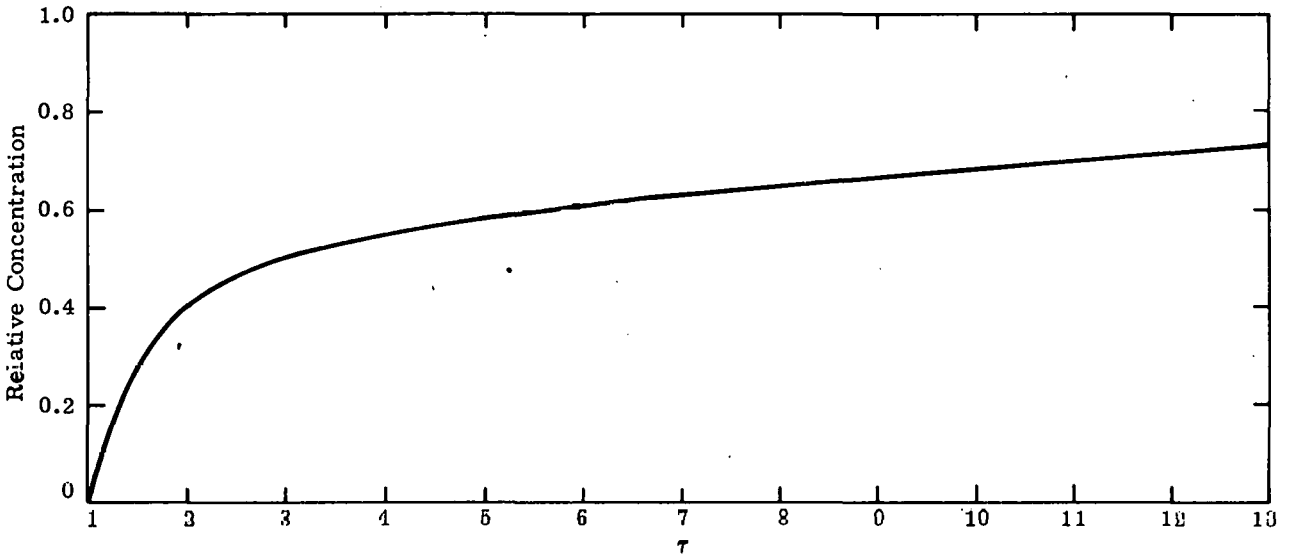

(a) For a Step Input of Tracer

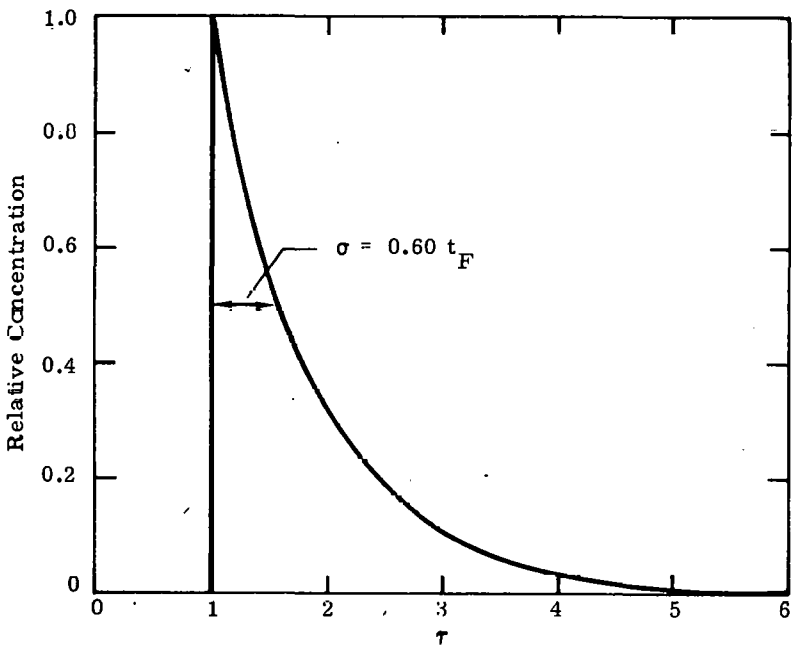

(b) Pulse Input of Tracer

Figure 19. Relative Concentration in the Recovery Well

and

$$t_F = \sigma / 0.60 \tag{58}$$

Equations (57) and (58) can be used to compute t_F when data is intermittent and pulse spreading is not evident. The pulse divergence exhibited by planar flow is inherent in the makeup of the flow geometry. It is not due to boundary effects in the flow paths or dispersion.

Active Void Volume

The active void volume (i.e., the total void volume less "dead" volume) along each path, v_j, can be determined from the q_j values and the mean arrival times, MAT_j, of the tracer peaks. The mean arrival time is calculated as

$$MAT_j = \frac{\int_o^\infty b_j(t)t\,dt}{b_{jT}} \quad . \tag{59}$$

The active void along the j^{th} path in a region is then

$$v_j = \left(MAT_j - MWT\right) q_j \quad . \tag{60}$$

The term MWT refers to the transit time of the tracer down the injection wellbore. (This factor is normally negligible, but can become important if the injector is substantially above the region of interest, if wellbore pressures are high, or if the wellbore diameter is very large.) The wellbore transit time can be given as

$$MWT = \sum_{k'=1}^{k} \frac{v_w^{k'}}{Q_{inj}^{k'}} \tag{61}$$

$v_w^{k'}$ and $Q_{inj}^{k'}$ are, respectively, the wellbore volume and injection well flow rate for each distinct region of the injection wellbore where $Q_{inj}^{k'}$ does not change significantly. That is, the actual wellbore flow will change with depth as flow goes out into the formation, and $Q_{inj}^{k'}$ and $v_w^{k'}$ are the appropriate values in each of the k regions between those changes. Generally, these values must be estimated values, based on interpretation of recovery-well data.

In practice, the mean arrival time in Eq (59) is calculated by truncating the integral at a finite upper limit (t_c). The value of t_c chosen will affect the size of the region which contributes to the flow. Figure 20 displays the bounding streamlines for two truncated flows and the equivalent output-tracer pulses.

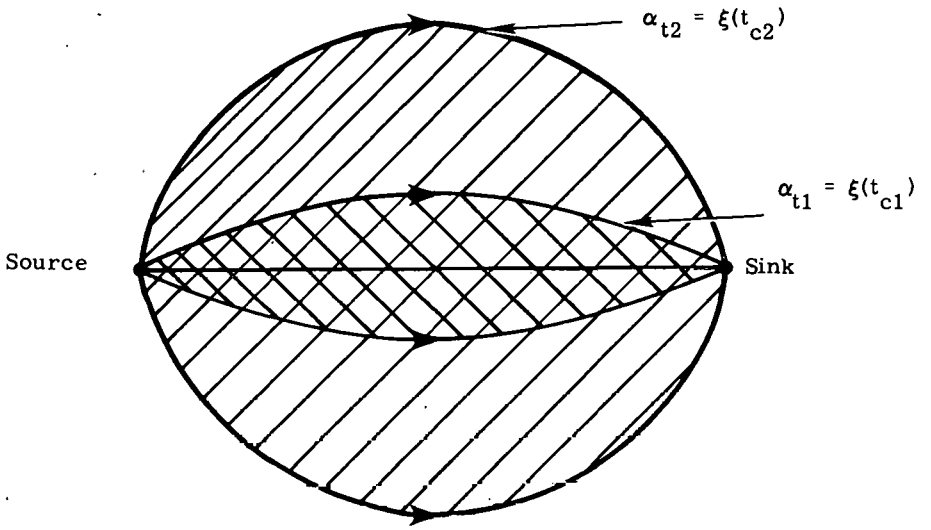

(a) Streamlines Bounding the Active Void Volume

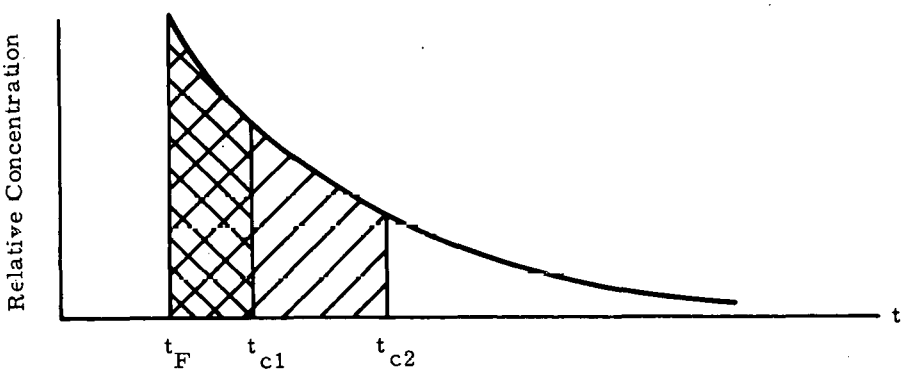

(b) Equivalent Areas Under the Tracer Output Curve

Figure 20. Boundaries of Active Void Volume and Equivalent Output Tracer Pulse for Two Cutoff Times (shaded areas)

Only flow that travels between streamlines that have a value $\leq \alpha_t^*$ (Figure 18) can contribute to the mean arrival time in Eq (59). The shaded area in Figure 20 represents the bounded "active void volume." The size of the planar area can be estimated from the value of α_t, which in turn can be evaluated from Eq (52). Equation (52) would have to be solved recursively in this situation; that is, various values of α would be substituted in Eq (52) until a $t(\alpha)$ equal to t_c is found. This procedure could be included in a general data-reduction program or done by hand on a typical scientific pocket calculator.

*This holds for flow in the $y \geq 0$ half-plane. The streamline pattern is symmetric about $\alpha = \pi$. For the $y < 0$ half-plane, the flow is restricted to values of $\alpha \geq 2\pi - \alpha_t$.

Compressible Carrier Fluids -- The data analysis techniques developed in this report are for incompressible flow. For techniques based on velocity or time of travel, the assumption of constant density could result in sizeable errors when gas carrier fluids are used in fractured formations that have a very low resistance to flow (small value of N), even if average densities are used in the computations. Test conditions requiring corrections and the magnitude of these correction factors are given in this section.

For channel flow, the general incompressible flow equation is

$$P_1 - P_2 = \frac{fLV^2\bar{\rho}}{2R_H} \tag{63}$$

Compressible flow is bracketed by isothermal and adiabatic conditions. The isothermal channel-flow equation is

$$P_1^2 - P_2^2 = \frac{fL(V\rho)^2 RT}{M_m R_H}\left(1 + \frac{2R_H}{fL}\ \ell n\ \frac{P_1}{P_2}\right) \tag{64}$$

and the adiabatic-flow equation is

$$\left(1 - \gamma\right)\frac{dV}{V} - \left[\frac{2\gamma P_1}{\rho_1} + \left(\gamma - 1\right)V_1^2\right]\frac{dV}{V^3} + \frac{\gamma f}{R_H}\,dx = 0\ . \tag{65}$$

Equation (65) was solved by Lapple. Parametric results are given in Reference 20. In the range of variables of interest, adiabatic-flow velocities are only slightly higher than those for isothermal flow. Therefore, correction factors will be computed only for isothermal flow, which can be solved algebraically. Assuming perfect gas,

$$\frac{1}{P_1 + P_2} = \frac{M_m}{2RT\bar{\rho}} \tag{66}$$

can be substituted into Eq (64) to yield

$$P_1 - P_2 = \frac{fL\bar{V}^2\bar{\rho}}{2R_H}\left(1 + \frac{2R_H}{fL}\ \ell n\ \frac{P_1}{P_2}\right)\ . \tag{67}$$

The ratio of incompressible to compressible flow velocities can then be found by equating Eqs (63) and (67).

$$\frac{V_I}{V_C} = \left(1 + \frac{2R_H}{fL}\ \ell n\ \frac{P_1}{P_2}\right)^{\frac{1}{2}} \tag{68}$$

provided

$$G \leq \sqrt{\frac{P_1 \rho_1}{2.72}} \tag{69}$$

which is the critical (theoretical maximum) mass velocity for compressible isothermal flow.

For any pressure gradient and frictional resistance, incompressible flow equations predict higher velocities. The percentile errors from using incompressible theory for gas flow methods were computed using Eq (68); the results are plotted in Figure 21. This figure can be used to determine when incompressible theory can be used. It can also be used to correct for compressibility effects as can Eq (68). Examples of some typical frictional resistances are given in Table 3.

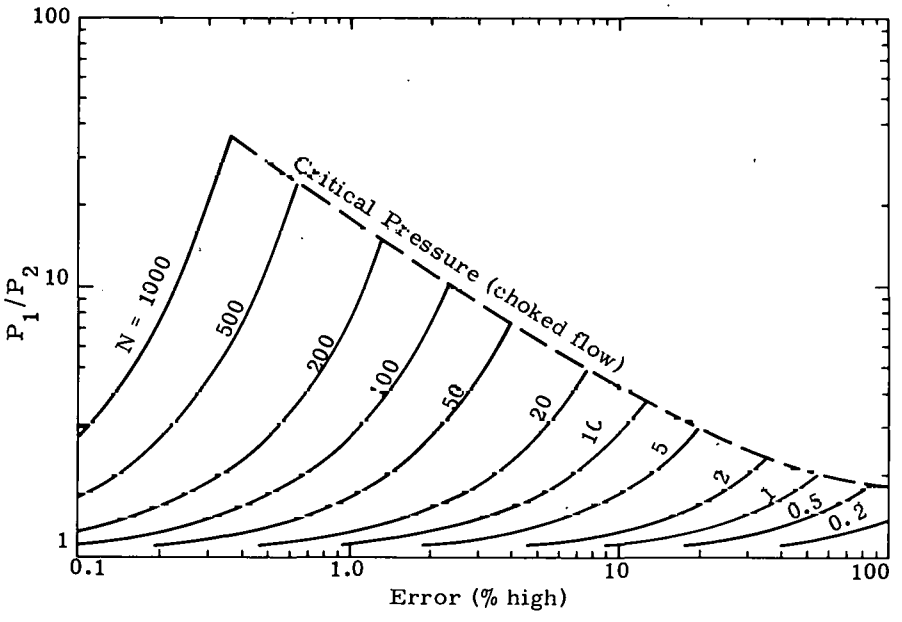

Figure 21. Velocity Errors From Using Incompressible Flow Equations and Mean Density for Isothermal Compressible Flow. $N = fL/R_H$

Table 3

Typical Frictional Resistances

Flow Path	N
Rough crack, 0.05 in. thick, 20 ft long	175
Smooth crack, 0.1 in. thick, 20 ft long	30
Smooth 2-in. pipe, 20 ft long	2.5

Compressibility effects are not as large for packed beds (rubbled formations) but must be considered for large size rubble with large void fractions. From Reference 20, the compressible-flow equation for packed beds is

$$P_1^2 - P_2^2 = \frac{2ZRG^2T}{M_m}\left[\ell n \frac{\rho_1}{\rho_2} + \frac{2f'L(1-\epsilon)^{3-n}}{\Phi^{3-n}\epsilon^3 D}\right] . \tag{70}$$

Using the mean density, the equation-of-state, and equating to Eq (63), the ratio of incompressible to compressible-flow velocities in rubbled media is

$$\frac{V_I}{V_C} = 1 + \frac{\Phi^{3-n}\epsilon^3 D}{2f'L(1-\epsilon)^{3-n}} \ell n \frac{P_1}{P_2} . \tag{71}$$

For all cases of interest, compressibility effects need not be considered for porous formations. This can be shown as follows: Darcy's law for incompressible flow with pure viscous drag is

$$P_1 - P_2 = \frac{\mu LV}{k} . \tag{72}$$

From Reference 20, the corresponding compressible-flow equation is

$$P_1^2 - P_2^2 = \frac{2RTV\rho L}{M_m}\left[\frac{\mu}{k} + \frac{V\rho}{L} \ell n \frac{P_1}{P_2}\right] \tag{73}$$

which can be rewritten, using Eq (66) as

$$P_1 - P_2 = \frac{\mu LV}{k}\left[1 + \frac{V\rho k}{L\mu} \ell n \frac{P_1}{P_2}\right] \tag{74}$$

and the velocity ratios in porous media is

$$\frac{V_I}{V_C} = 1 + \frac{V\rho k}{L\mu} \ell n \frac{P_1}{P_2} . \tag{75}$$

Solutions to Eq (75) are equal to unity to within four significant figures for all test conditions likely to be encountered in porous media.

Ratios of velocities using an incompressible fluid to those using a compressible fluid are given in Eq (68) and Figure 21 for flow in fractures, in Eq (71) for packed beds, and in Eq (75) for porous media.

Mechanical Dispersion in Porous Media -- Hydrodynamic dispersion in porous media can significantly alter the shape of the ideal recovery well pulse (Figure 19 (b)); the successful reduction of tracer test data may hinge upon the magnitude and effect of this dispersion. All previous data reduction has assumed that t_F and the time of maximum concentration (t_{max}) coincide. This may not be true when dispersion is present. This section mathematically describes dispersion of the tracer pulse and discusses its effect on data analyses. As before, the dispersive media are assumed to be isotropic and homogeneous in the xy plane.

An approximate solution to the convection-dispersion equation for a source-sink configuration is given in Reference 21. This solution is for dispersion parallel to the velocity vector; that is, no net flow across streamlines is allowed in this approximation. The concentration for an instantaneous injection of tracer of mass M is

$$C(\tau,\alpha) = \frac{M}{2\rho Q\sqrt{\pi\sigma(\alpha)}} \exp\left[-(a(\alpha) - \tau)^2/4\sigma(\alpha)\right] \tag{76}$$

where

$$\begin{aligned} a(\alpha) &= 1 && \alpha = 0, 2\pi \\ a(\alpha) &= 3\,\frac{1 - \alpha\cot\alpha}{\sin^2\alpha} && 0 < \alpha < 2\pi \end{aligned} \tag{77}$$

and

$$\begin{aligned} \sigma(\alpha) &= 4\beta/15 && \alpha = 0,\ 2\pi \\ \sigma(\alpha) &= \beta\csc^4\alpha\,[\alpha\sin\alpha - 3\cos\alpha\,(1 - \alpha\cot\alpha)]. && 0 < \alpha < 2\pi \end{aligned} \tag{78}$$

β is a dispersion parameter which is directly proportional to the mean grain size of the dispersive media and inversely proportional to the well spacing.[22] As β approaches 0, the effects of dispersion become negligible.

Equation (76) gives the results for any one streamline identified by angle α. To include the effects of divergence, the solution for dispersion must be integrated over the streamline angle. The full solution becomes

$$C(\tau) = \frac{M}{2\rho Q\sqrt{\pi}} \int_0^{2\pi} \exp\left[-(a(\alpha) - \tau)^2/4\sigma(\alpha)\right] \Big/ \sqrt{\sigma(\alpha)}\ d\alpha \tag{79}$$

with $a(\alpha)$ and $\sigma(\alpha)$ as defined in Eqs (77) and (78), respectively. The use of τ (time relative to t_F) makes Eq (79) applicable to all geometries. The site-dependent information is contained in β and t_F.

The concentration at the output well is plotted versus τ for a variety of β's. Figure 22 shows C versus τ for β = 0.1, 0.01, and 0.001, respectively. These figures show that t_{max} and t_F do not coincide. Figure 23 shows the relationship between t_{max}/t_F and β. As $\beta \to 0$, the effects of dispersion become negligible; t_{max}/t_F tends towards unity and the decay constant approaches $1.16/t_F$.

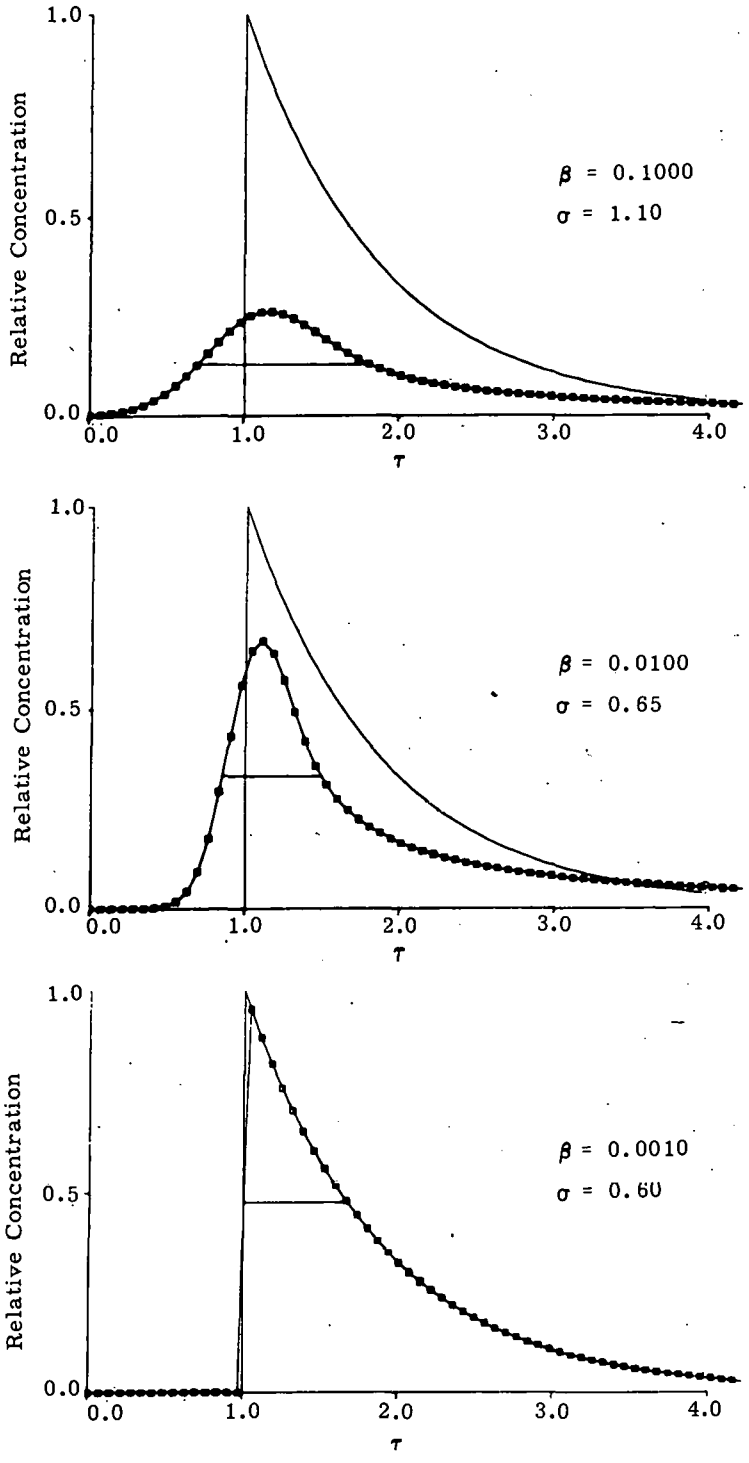

Figure 22. Spreading Due to Dispersion Along Streamlines

If an estimate of β could be made, t_F can be found from Figure 23 using t_{max}. Otherwise, a least squares fit of experimental data to Eq (79) could be made. This fit would predict values for β and t_F with no additional information. If a dual fit cannot be made, a rough estimate of t_F would be 0.9 t_{max}. This estimate would probably be accurate to ±10%. The derivation described here does not include any molecular diffusion processes. The diffusion constant for typical molecular processes is approximately three orders of magnitude smaller than an equivalent dispersion constant. Therefore, the possible pulse alteration by diffusion should be negligible compared with the alteration caused by mechanical dispersion.

Once t_F is known, the techniques described in the "Divergence of Streamlines" section can be used for data analysis.

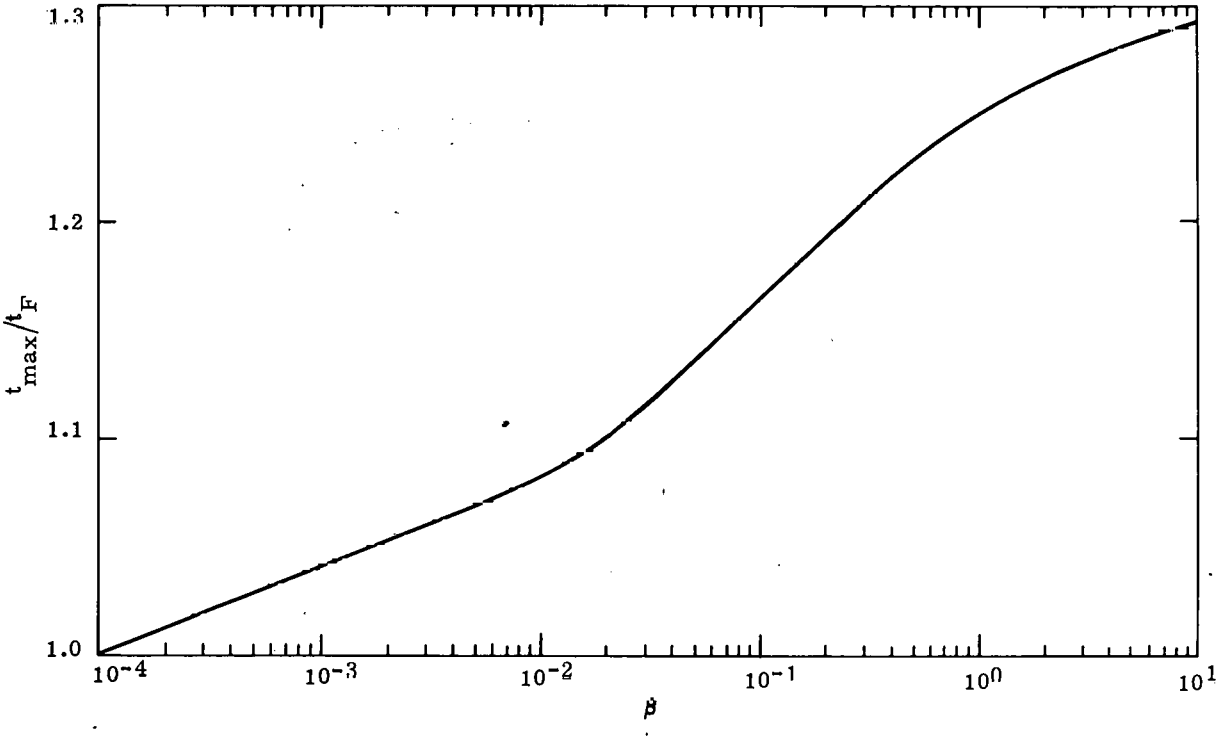

Figure 23. Variation of t_{max} With Dispersion Parameter β

Pulse Spreading -- Spreading of the tracer pulse, as seen in the recovery well, can be caused by the test configuration as well as by flow through the formation. One cause of particular interest to the tracer-test system is discussed here.

If a permeable region of thickness D exists between the input and output well, there would be a reduction in velocity as a tracer pulse moves down the input well caused by flow into the formation. This velocity change, coupled with a longer flow path in the injection well, would cause later arrival times of the tracer at the output well with increasing depth. This configuration is described in Figure 24.

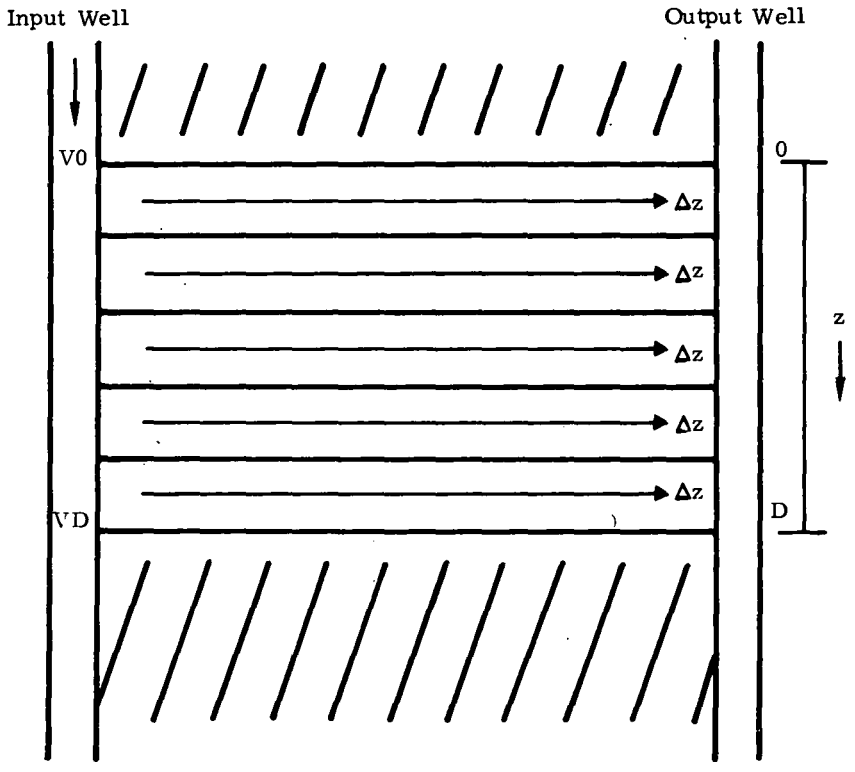

$V(z) = (V0 - VD)(1 - z/D)$
V0 = Flow velocity at top of region
VD = Flow velocity at bottom of region
D = Thickness of permeable region

Figure 24. Permeable Region in a Two-Well Flow Test

For measurements above the permeable region, the concentration in the recovery well can be represented by

$$C(\tau) = C_o \sum_{n=0}^{D/\Delta z} \left[\exp -\lambda \left(\tau - 1 - \frac{zn\Delta z}{t_\Gamma V(n\Delta z)} \right) \right] \tag{80}$$

and

$$V(z) = V0 \left[1 - \left(VD/V0 - 1 \right) z/D \right] . \tag{81}$$

The planar flow characteristics are the same for each level of the permeable region as $\Delta z \rightarrow 0$, that is λ and C_o are not functions of z. The sum can be transformed into an integral by allowing Δz to become infinitesimal and replacing it with dz. Equation (80) becomes

$$C(\tau) = 0 \qquad \tau < 1$$

$$C(\tau) = C_o \exp\left[-\lambda(\tau - 1)\right] \int_0^{z_\tau} \exp\left[2\lambda z / t_F V(z)\right] dz$$

$$= C_o \exp\left[-\lambda(\tau - 1)\right] \left\{ \int_0^{u_\tau} \exp\left[\frac{2\lambda D}{t_F V0} \cdot \frac{u}{1 + (VD/V0 - 1)u}\right] du \right\} . \qquad (82)$$

Where the replacement $u = z/D$ has been made and Eq (81) substituted for V(z). Two sets of constants define the concentration as a function of τ for this configuration. They are VD/V0 and $D/t_F V0$. The first is the ratio of velocities in the input well; the second is a measure of the time it takes a tracer pulse to travel by the permeable region relative to t_F. The upper limit of integration depends on τ; that is, the integration is carried out only to include those planar flow paths that can be reached in a distance u_τ. The time it takes to get to a depth z can be determined by integrating Eq (81). This gives

$$\tau(z) = \frac{D}{t_F V0 (VD/V0 - 1)} \ln\left[1 + (VD/V0 - 1) z/D\right] , \qquad (83)$$

which can be inverted to give z/D as a function of τ. This gives

$$u_\tau = z_\tau / D = \frac{1 - \exp\left[\tau t_F V0 (VD/V0 - 1)/D\right]}{1 - VD/V0} . \qquad (84)$$

As time advances, the tracer reaches progressively lower flow paths and the upper limit of integration increases to a maximum of 1 when $z_\tau = D$.

A wide range of values for $D/t_F V0$ and VD/V0 were analyzed parametrically. The output-well concentrations are plotted as a function of $\bar{\tau}$. Four graphs, which bracket most test conditions, are displayed in Figure 25.

The time of the maximum concentration (t_{max}) and the full width at half-maximum (σ) were used to analyze the curves. Figure 26(a) shows σ as a function of VD/V0 for constant values of $D/t_F V0$. Figure 26(b) shows t_{max} for the same situation. The parametric study shows that Figure 25(d) represents the maximum output distortion and spreading caused by a porous region for any formation properties and any test configuration. This is substantiated by Figure 26.

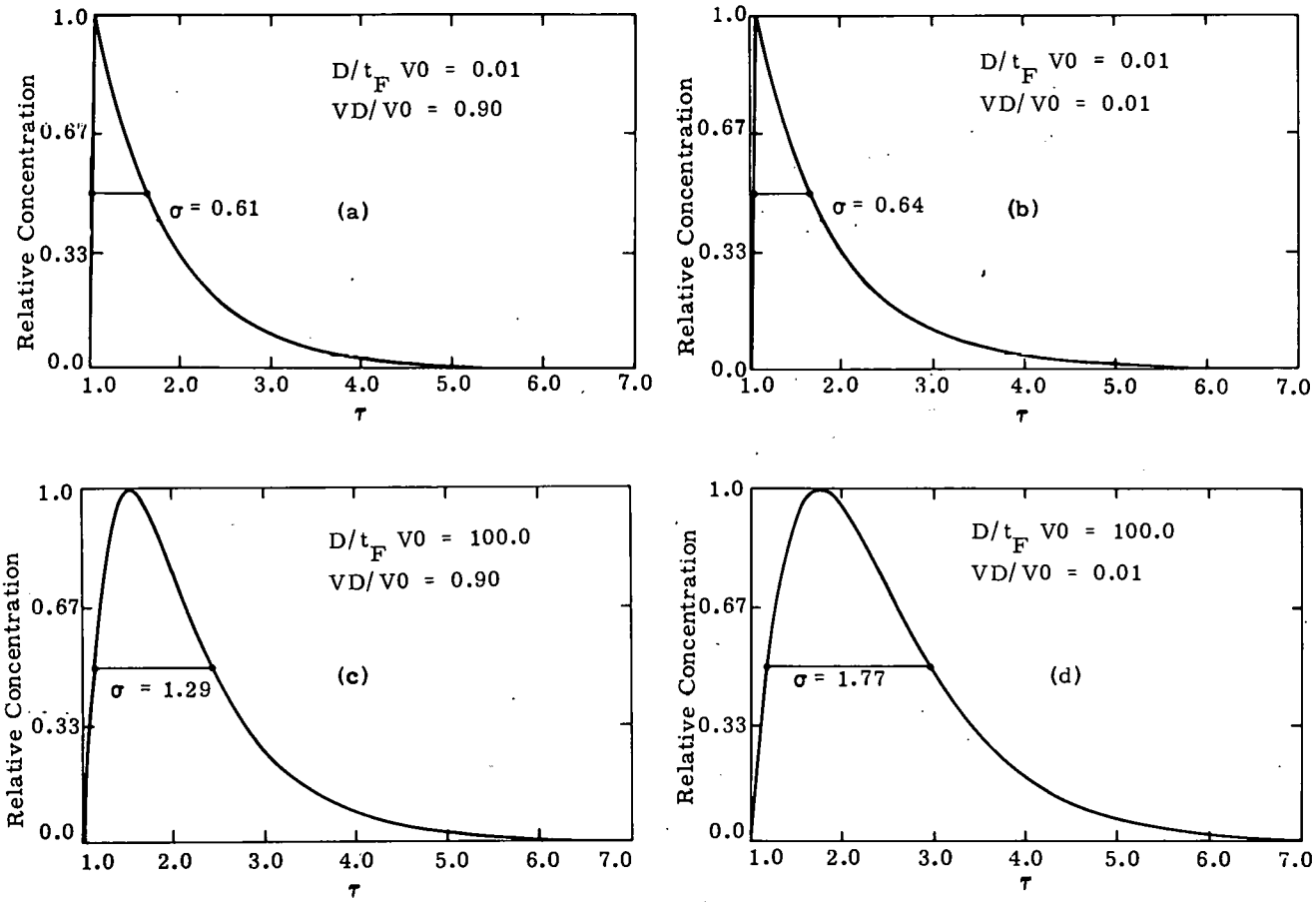

Figure 25. Pulse Spreading in Recovery Well Due to a Permeable Region

This theoretical treatment does not include dispersion. Dispersion alone produces a spreading mainly centered around t_F, whereas spreading from a permeable region is shifted towards higher τ's. Given a graph of experimental data with no other information, it would be difficult to specify the value of t_F and the cause of spreading. Porous regions can be identified using one of the flow logging methods discussed earlier in this report. In addition, data analysis can be simplified by minimizing pulse spreading. This can be accomplished to some degree by designing experiments in porous media to minimize $D/t_F V0$. Smaller diameter wells and increased flow rates increase V0; larger well spacing increases t_F. It is not possible to increase VD/V0 experimentally. VD/V0 depends on the quantity of the flow below the permeable region. As can be seen in Figure 26(b), t_F can be closely approximated by $0.9\ t_{max}$ if $D/t_F V0$ is kept below 0.1.

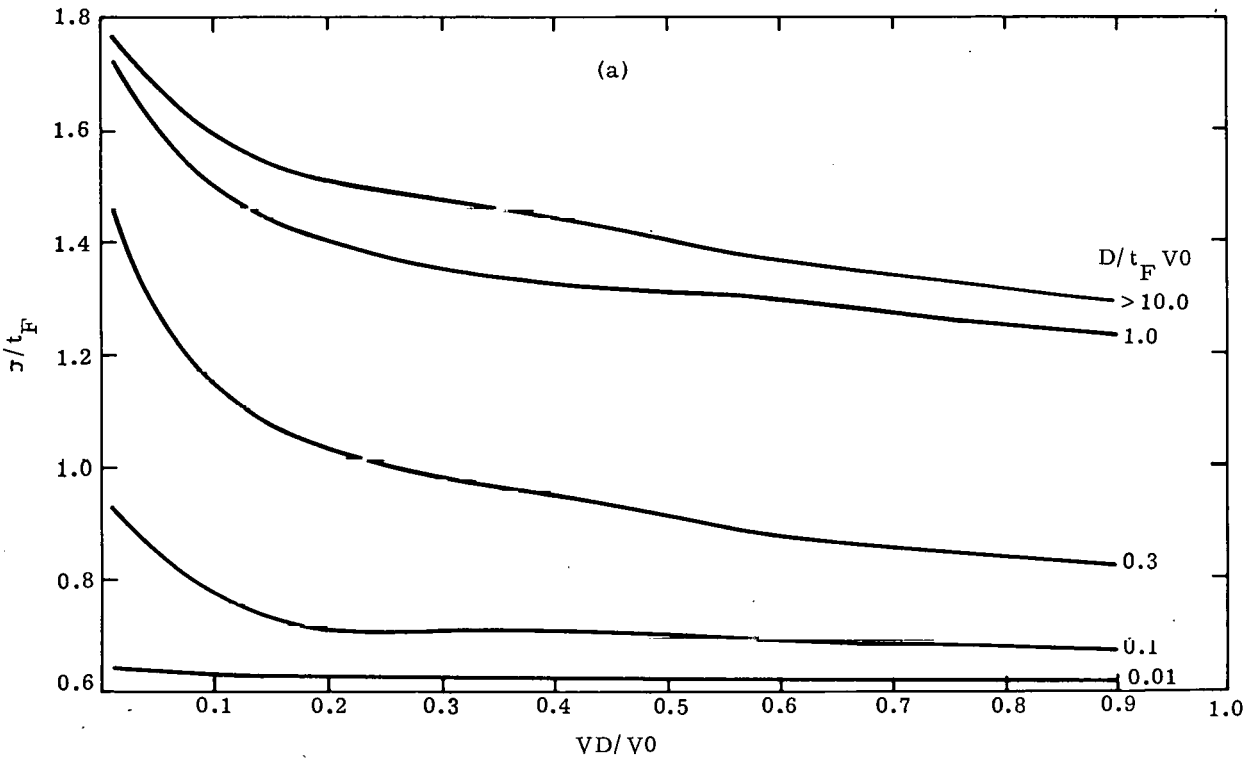

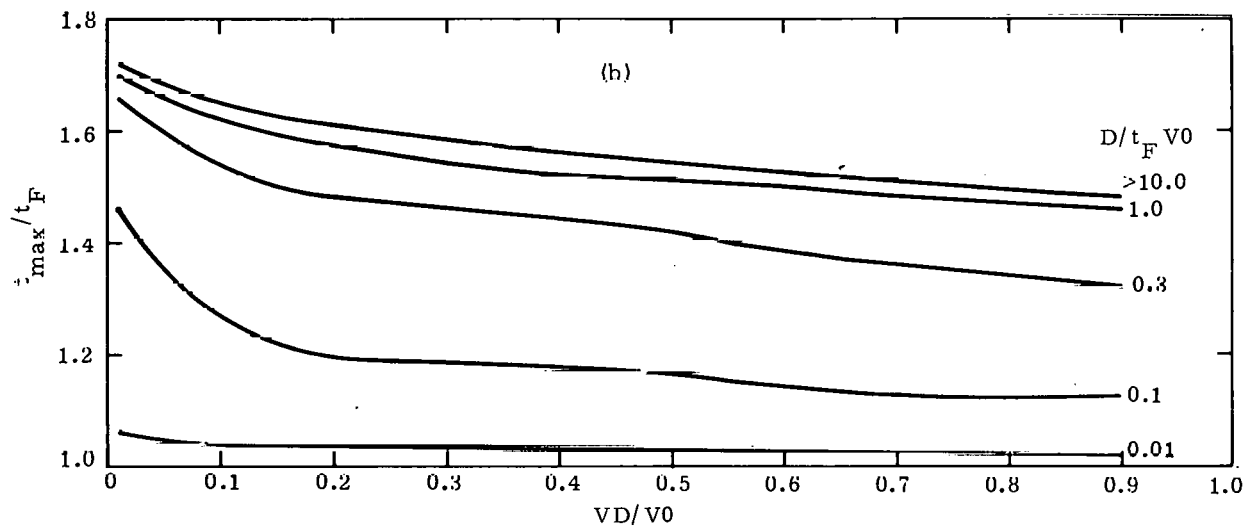

Figure 26. Functions of VD/V0 for a Permeable Region

Confined Flow

All previous derivations of flow properties have assumed semiinfinite media, bounded only by impermeable layers parallel to the flow. Many experimental configurations, such as thermally or mechanically altered zones, are confined on all sides. The derivations in the "Divergence of Streamlines" and "Pulse Decay Characteristics in the Recovery Well" sections are repeated for a configuration with impermeable boundaries at finite distances from the input and recovery wells. A rectangular bound region was chosen to approximate experimental conditions. This configuration is described in Figure 27. The rectangle has a length of $2L_H$ and a width of $2W_H$, the position of the input well is x1, y1 and the output well is x2, y2. There are no restrictions on the positions of the two wells; any value of x and y less than L_H and W_H are allowed. Laplace's equation ($\nabla^2\Phi = 0$) in two dimensions governs the form of the velocity potential for frictionless flow. Laplace's equation with linear boundary conditions is easily solvable by the method of images and superposition.[23]

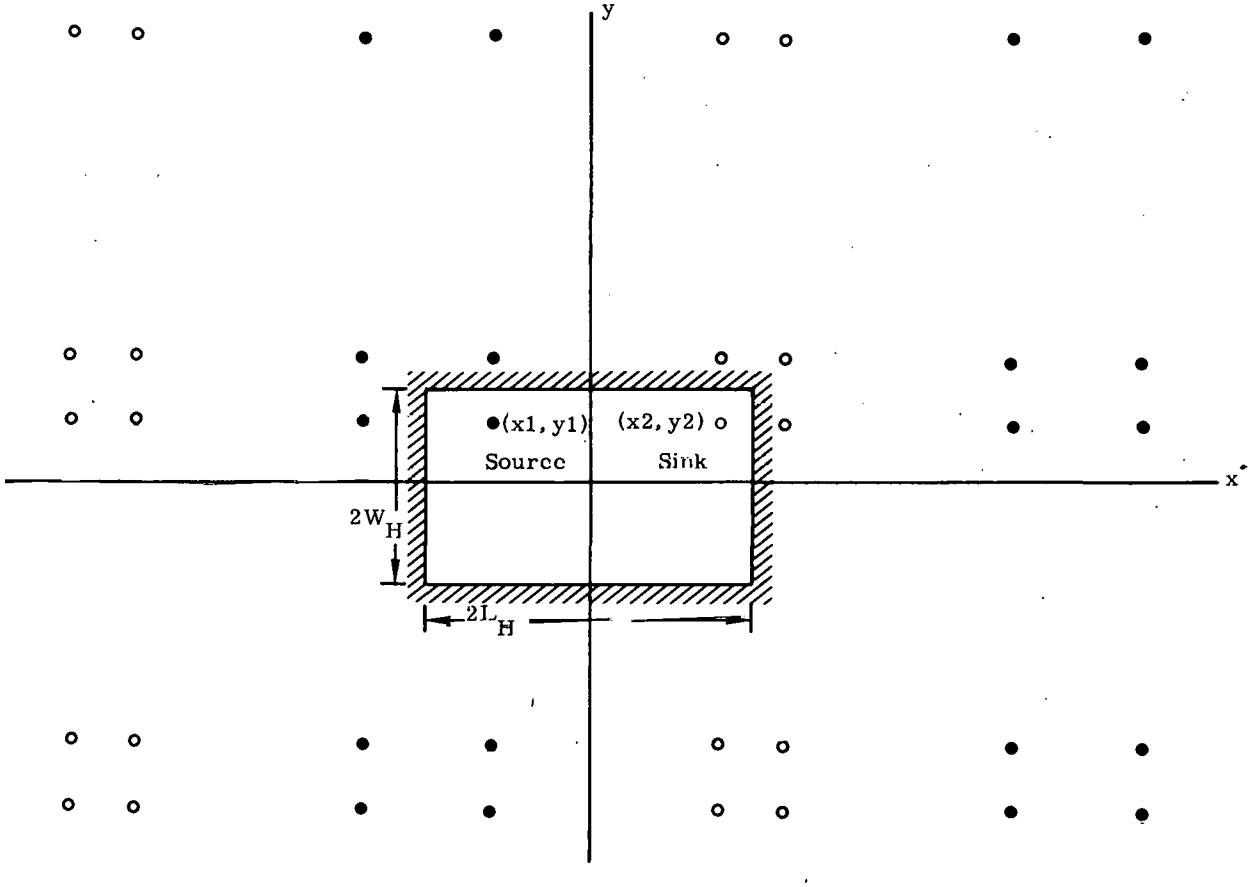

Figure 27. Layout of Sources and Sinks for a Rectangular Confined Region

To get a feel for how the images are laid out, consider an infinite strip of width $2W_H$ with a source of sink y1, away from the axis. The coordinates of the real and imaginary sources or sinks are

$$Y_1 = 2(2n1 - 1)W_H - y1$$
$$Y_2 = 4n2\,W_H + y1 \tag{85}$$

where n2 = 0 represents the position of the real source or sink. The velocity potential for geological flow is proportional to $\ell n\ r$ where r is the distance from the point of measurement to the source or sink. For the infinite strip, the total potential is a sum over all source or sink positions

$$\Phi(x,y) = \frac{q}{2\pi}\sum_{n=-\infty}^{\infty} \ell n\left[\left(y - 2\left(2n + 1\right)W_H + y1\right)^2 + x^2\right]^{\frac{1}{2}} + \ell n\left[\left(y - 4nW_H - y1\right)^2 + x^2\right]^{\frac{1}{2}} \tag{86}$$

using the positions from Eq (85). Superposition of two infinite strips perpendicular to each other will produce a doubly infinite set of image sources or sinks. The final step is to superimpose a source and a sink in the confined region (Figure 27). The velocity potential for this configuration is

$$\begin{aligned}\Phi(x,y) = \frac{q}{2\pi}\sum_{n=-\infty}^{\infty}\sum_{m=-\infty}^{\infty} &\ell n\left\{\left(2\left(2m + 1\right)L_H - x2 - x\right)^2 + \left(2\left(2n + 1\right)W_H - y2 - y\right)^2\right\}^{\frac{1}{2}} \\ &+ \ell n\left\{\left(2\left(2m + 1\right)L_H - x2 - x\right)^2 + \left(4nW_H + y2 - y\right)^2\right\}^{\frac{1}{2}} \\ &+ \ell n\left\{\left(4mL_H + x2 - x\right)^2 + \left(2\left(2n + 1\right)W_H - y2 - y\right)^2\right\}^{\frac{1}{2}} \\ &+ \ell n\left\{\left(4mL_H + x2 - x\right)^2 + \left(4nW_H + y2 - y\right)^2\right\}^{\frac{1}{2}} \\ &- \ell n\left\{\left(2\left(2m + 1\right)L_H - x1 - x\right)^2 + \left(2\left(2n + 1\right)W_H - y1 - y\right)^2\right\}^{\frac{1}{2}} \\ &- \ell n\left\{\left(2\left(2m + 1\right)L_H - x1 - x\right)^2 + \left(4nW_H + y1 - y\right)^2\right\}^{\frac{1}{2}} \\ &- \ell n\left\{\left(4mL_H + x1 - x\right)^2 + \left(2\left(2n + 1\right)W_H - y1 - y\right)^2\right\}^{\frac{1}{2}}\end{aligned} \tag{87}$$

$$- \ell n \left\{ \left(4mL_H + x1 - x\right)^2 + \left(4nW_H + y1 - y\right)^2 \right\}^{\frac{1}{2}} \quad . \tag{87}$$

The streamlines can be defined in a similar way; they are

$$\begin{aligned}
\Psi(x,y) = \frac{q}{2\pi} \sum_{n=-\infty}^{\infty} \sum_{m=-\infty}^{\infty} & \tan^{-1} \left\{ \frac{y - 2(2n+1)W_H + y2}{x - 2(2m+1)L_H + x2} \right\} + \tan^{-1} \left\{ \frac{y - 4nW_H - y2}{x - 2(2m+1)L_H + x2} \right\} \\
& + \tan^{-1} \left\{ \frac{y - 2(2n+1)W_H + y2}{x - 4mL_H - x2} \right\} + \tan^{-1} \left\{ \frac{y - 4nW_H - y2}{x - 4mL_H - x2} \right\} \\
& - \tan^{-1} \left\{ \frac{y - 2(2n+1)W_H + y1}{x - 2(2m+1)L_H + x1} \right\} - \tan^{-1} \left\{ \frac{y - 4nW_H - y1}{x - 2(2m+1)L_H + x1} \right\} \\
& - \tan^{-1} \left\{ \frac{y - 2(2n+1)W_H + y1}{x - 4mL_H - x1} \right\} - \tan^{-1} \left\{ \frac{y - 4nW_H - y1}{x - 2(2m+1)L_H + x1} \right\} \quad .
\end{aligned} \tag{88}$$

The velocity of the flow is defined in terms of the velocity potential $\Phi(x,y)$ for a porous medium

$$V_x = -\frac{1}{\epsilon} \frac{\partial \Phi}{\partial x} \quad \text{and} \quad V_y = -\frac{1}{\epsilon} \frac{\partial \Phi}{\partial y} \quad . \tag{89}$$

Conceptionally, all the information to characterize a confined region is available. However, the equations cannot be solved analytically as with unconfined flow. A functional form for the travel time of a tracer for any given streamline has not been found for the confined flow problem. The time of first arrival in a confined region (t_{FC}) has to be calculated numerically for each configuration. The shortest distance between wells is not necessarily the path for the shortest flow time; these only coincide when the boundaries are symmetric about the bisector of the two wells.

The computer program CONFLOW[24] was written to integrate $1/V_x$ along any streamline x1 to x2 for the confined flow problem. This program uses Eqs (87) and (88) to calculate the velocity and position of the streamline. The sums that appear in these equations are truncated at n = m = 7. It was found that this value for m and n produced a boundary accurate to 1% of the total extent; that is, if the bound region for the ∞ series was supposed to be $2L_H$ by $2W_H$, the region predicted by the truncated series would be within 1% of this area. Since experimental error in a real flow test is much larger than this and altered boundaries are not straight-sided rectangles, the truncated series is considered adequate.

Figure 28 shows typical flow patterns for six sets of well positions and boundaries. The distortions of the streamlines, due to confinement, are evident in these figures. A series of parametric computer models was run for the confined flow problem. The ratio of the length (L_H) to the width (W) of the confined region was varied from 5:5 to 5:2; y1 was equal to y2 and x1 was equal to minus x2 for all models (Figures 28d, e, f). The ratio $x1/L_H$ took on values of 0.2, 0.4, 0.6, and 0.8. The values of $y1/W_H$ varied with the aspect ratio of the confined region. The time of first arrival (t_{FC}) for the confined region is compared to t_F from the "Divergence of Streamlines" section for the same separation. Figure 29 displays the curves of t_{FC}/t_F as a function of $x1/L_H$ for constant $y1/W_H$. The values of this ratio tend toward 1 as $x1 \to 0$, with transit times less in confined regions as expected. Other test configurations such as those shown in Figure 28b and c can be modeled using the computer program CONFLOW.

One of the inputs to data analyses of confined flow is the value of t_{FC} measured during the test. An equivalent value for t_F can be calculated from Figure 29 or the use of the program CONFLOW by dividing by the ratio t_{FC}/t_F. This value of t_F is used for subsequent data analyses. If q is known from the data reduction, then the porosity for $a \ll S$ can be determined using Eq (39). A determination of K requires information concerning the change in pressure for a confined flow region. This pressure drop can be represented by

$$\Delta P = \frac{\rho g}{K} \left\{ \Phi\left(x1 + a,\ y1\right) - \Phi\left(x2 - a,\ y2\right) \right\} \tag{90}$$

where $\Phi(x, y)$ is given by Eq (87) and a is much less than the well spacing. Equation (90) can also be written as

$$\Delta P = \frac{q\rho g}{2\pi K}\, \eta\left(x1, y1, x2, y2, L_H, W_H, a\right) \tag{91}$$

with

$$\eta\left(x1, y1, x2, y2, L_H, W_H, a\right) = \frac{2\pi}{q} \left\{ \Phi\left(x1 + a, y1\right) - \Phi\left(x2 - a, y2\right) \right\}. \tag{92}$$

Values for η are given in Figure 30 for the same set of parameters that were used in Figure 29. Values for η for other configurations can be found using the program CONFLOW. With q known, the hydraulic conductivity for confined flow can be found by inverting Eq (91). This is given by

$$K \simeq \frac{q\rho g}{2\pi \Delta P}\, \eta^{*}. \tag{93}$$

*The parameter list of the function η is dropped for brevity here and in subsequent derivations.

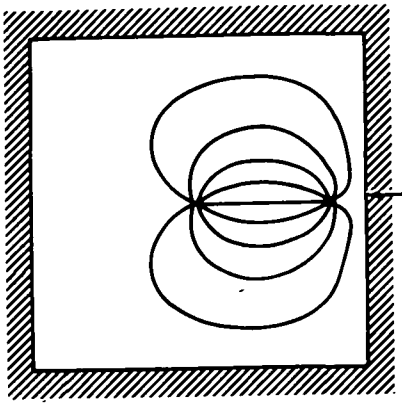

a. The y boundary is at +/- 100.00
The x boundary is at +/- 100.00
The sink is at 0.00 0.00
The source is at 80.00 0.00

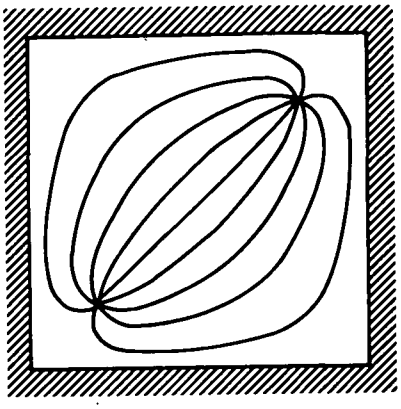

b. The y boundary is at +/- 100.00
The x boundary is at +/- 100.00
The sink is at -80.00 -80.00
The source is at 80.00 80.00

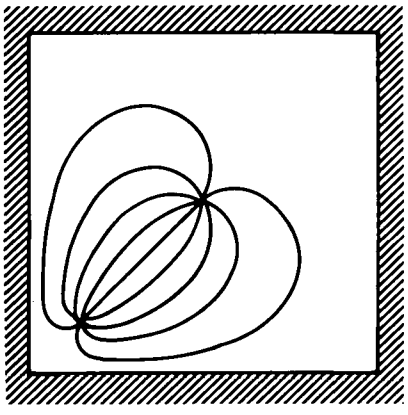

c. The y boundary is at +/- 100.00
The x boundary is at +/- 100.00
The sink is at 0.00 0.00
The source is at -80.00 -80.00

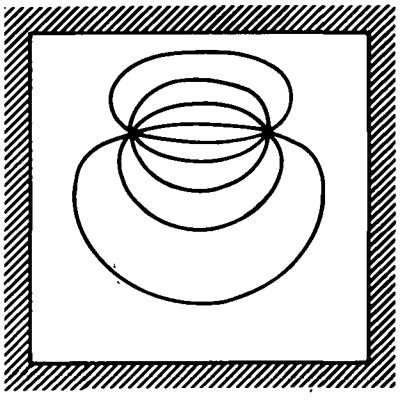

d. The y boundary is at +/- 100.00
The x boundary is at +/- 100.00
The sink is at -40.00 40.00
The source is at 40.00 40.00

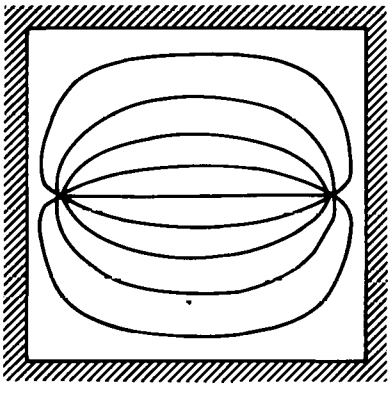

e. The y boundary is at +/- 100.00
The x boundary is at +/- 100.00
The sink is at -80.00 0.00
The source is at 80.00 0.00

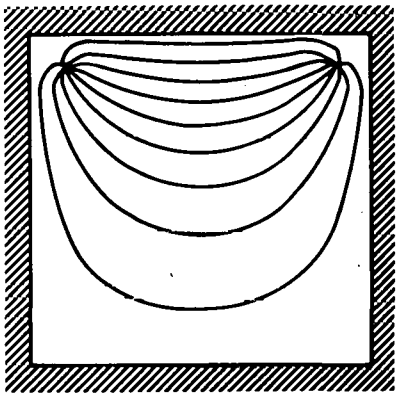

f. The y boundary is at +/- 100.00
The x boundary is at +/- 100.00
The sink is at -80.00 80.00
The source is at 80.00 80.00

Figure 28. Geologic Flow Streamlines for Confined Regions

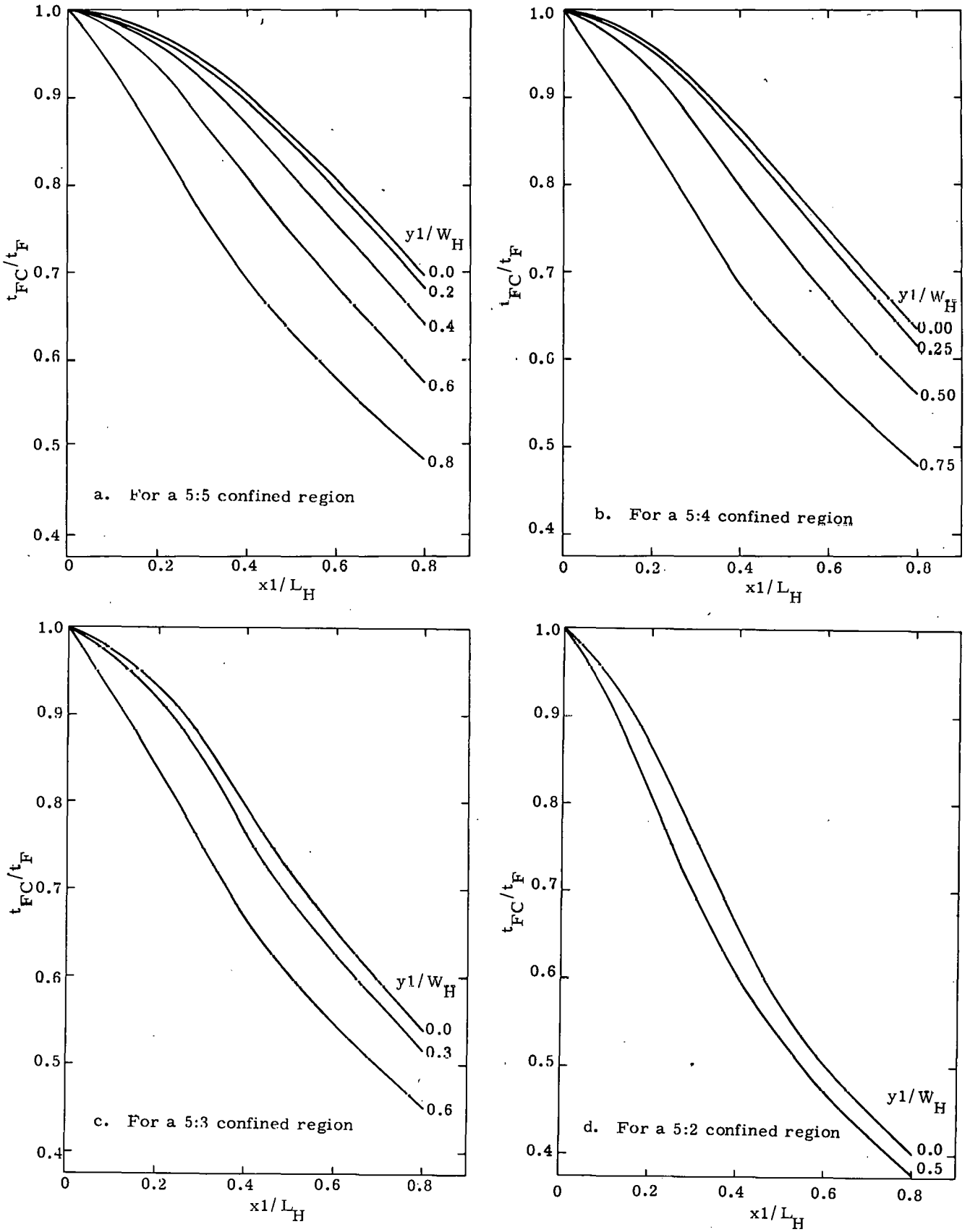

Figure 29. Relative Times of First Arrival for Confined Regions

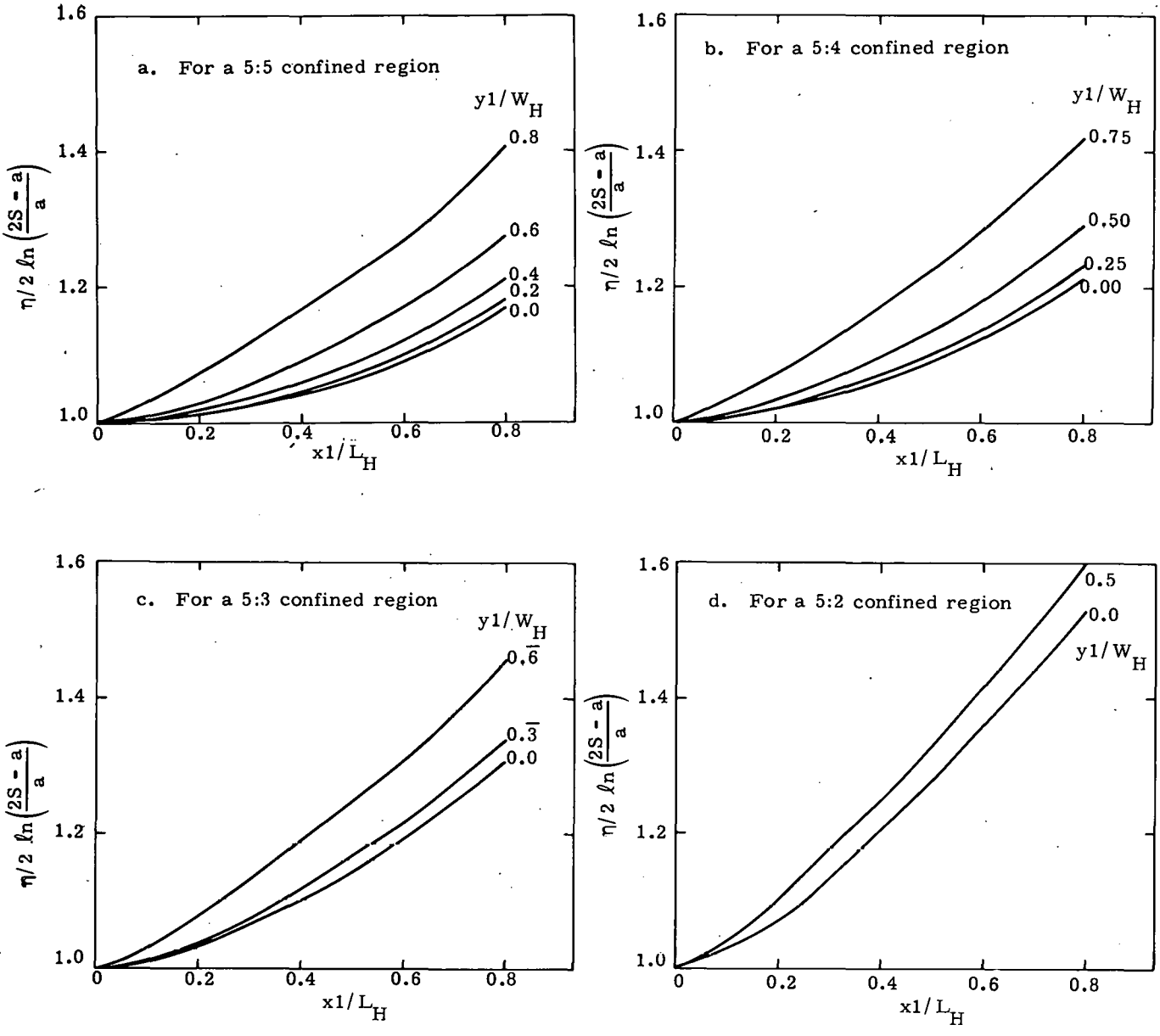

Figure 30. Relative Pressure Drops for Confined Regions

If the porosity can be estimated and q cannot be measured, the hydraulic conductivity can be found by using

$$K \simeq \frac{2\rho g S^2 \epsilon}{3\Delta P t_F} \eta \tag{94}$$

with

$$S = \frac{1}{2}\left[\left(x1 - x2\right)^2 + \left(y1 - y2\right)^2\right]^{\frac{1}{2}} \tag{95}$$

for confined flow and $a \ll S$. Equation (42), which represents the combined thickness of thin, porous layers between two detectors, can be used for confined flow with the values for the effective t_F and S (Eq (95)). The fracture thickness for laminar flow can be developed in the same manner as for unconfined flow, and is given by

$$h_L \simeq \left(\frac{16 S^2 \mu}{3 t_F \Delta P} \eta\right)^{\frac{1}{2}} \tag{96}$$

for $a \ll S$. If an estimate of the friction factor (Eq (44)) can be made, the fracture thickness for turbulent flow is given by

$$h_T \simeq \frac{4 f S^3 \rho}{3 t_F^2 \Delta P} \eta \tag{97}$$

for $a \ll S$. The frictional resistance of the fracture for turbulent flow is given by

$$N_T \simeq \frac{3 t_F^2 \Delta P}{4 S^2 \rho_{11}} \tag{98}$$

for $a \ll S$. For Eqs (94) through (98), the effective t_F and S must be used for all data analysis. In addition to computing the ratio t_{FC}/t_F and η, CONFLOW also produces a streamline plot showing boundaries and wells and a theoretical tracer-output plot showing the effects of divergence. The theoretical output plot is useful in analyzing actual output.

A set of models similar to those in the "Pulse Decay Characteristics in the Recovery Well" section was used to investigate the time-dependent flow characteristics of confined flow. The relative concentration with respect to τ was calculated for each model and this data was then fitted to the same decaying exponential form. In general, the fits were not very good. The short-time ($1 \leq \tau \leq 2$) characteristics were approximately exponential, but for times longer than 2 t_{FC} the relative concentration approaches a constant level (Figure 31). This seems to be a major effect in the confined configuration and has been seen in some field-test data.

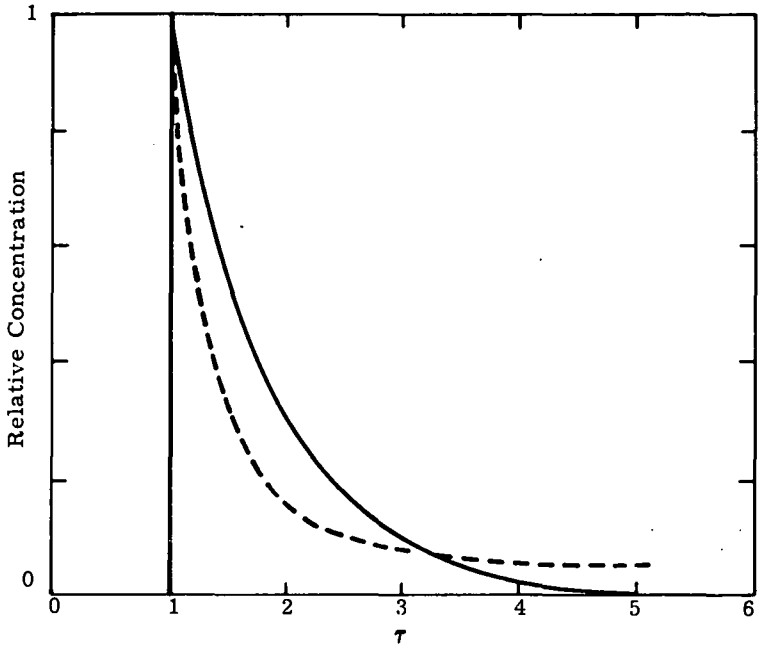

Figure 31. Comparison of Confined (- - -) and Unconfined (——) Decay Characteristics

Because the time development of the concentration for the confined problem is not a decaying exponential, the utility of a decay constant is limited. However, some qualitative trends can be reported. As the deviations from ∞ boundaries become greater, the decay constant (λ) increases. As the ratio of length to width of the confined region increases, the decay constant also increases. The parametric models do indicate that as x1/L approaches 0, the unconfined value of λ is approached.

The inclusion of dispersion was not attempted for the confined flow problem. It was felt that dispersion required a quantum increase in mathematical complexity with only a small increase in understanding of the effects. The spreading and shifting of t_{max} relative to t_F due to dispersion should be similar in both configurations. If dispersion is present, then some allowance should be made for the delay induced by this effect.

The tendency of the concentration in confined-flow problems to approach a constant value may be useful in determining whether confinement is present. If test wells are drilled in a region of unknown confinement, the recovery-well decay could be compared to the unconfined decay curve. A leveling off of concentration at long times would indicate a confined region. This could be due to a lens formation or some other vertical impermeable boundaries present.

The use of a rectangular confining region should not limit the utility of this procedure. Figure 32 displays two possible test layouts that can be modeled by rectangular impermeable boundaries. The large uncertainties in the size and shape of a geologic-confined region justifies the use of a rectangular approximation. Figure 28 can be helpful in laying out an experiment in a confined

region and as a guide for data analysis as illustrated in Figure 32.* t_{FC} is affected by the boundaries but is not very sensitive to the exact size and orientation of them. Figure 29 supports this argument.

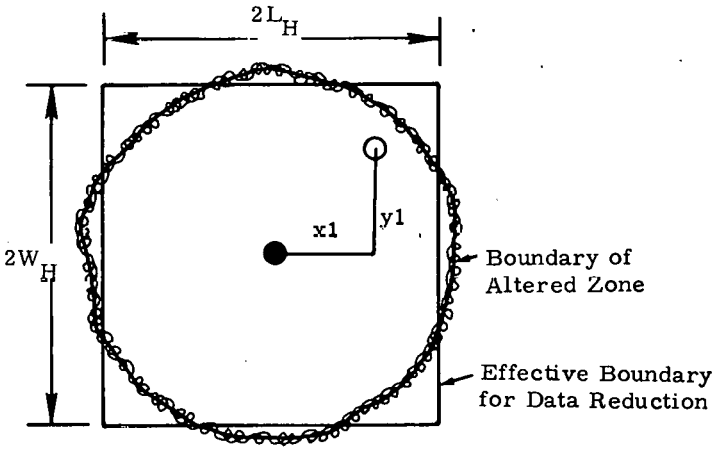

a. Flow Between Central (activation) Well and a Radial (sampling) Well

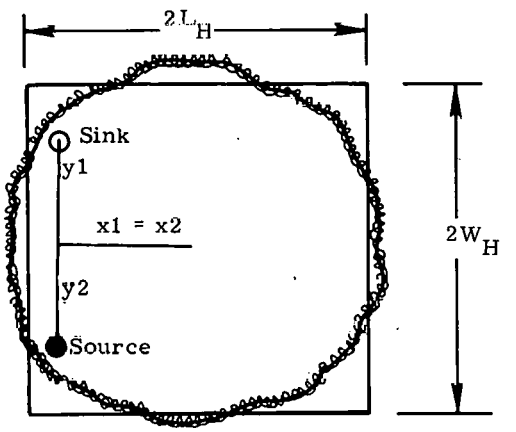

b. Flow Between Two Peripheral Wells

Figure 32. Confined Two-Dimensional Flow Approximation for a Circular Zone Altered Mechanically, Thermally, or Chemically

V. Data Analysis of Three-Dimensional Unconfined Flow

The two-well problem, where the wells are cased except for a small section at the bottom, can be approximated by a spherical source and sink, which requires a full three-dimensional solution of Laplace's equation. This section contains the derivation of equations needed to characterize a formation using three-dimension flow-test data.

Divergence of Stream Surfaces

The time of first arrival (t_{F3}) of a tracer is the basis for this data analysis. The equipotential and stream surfaces for a spherical source and sink are shown in Figure 33. The velocity potential is independent of ψ and equals

$$\Phi = \frac{Q}{4\pi}\left(\frac{1}{r_+} - \frac{1}{r_-}\right) \tag{99}$$

where Q is the total flow at the input well.[17] The two radii can be expressed in terms of r by the Law of Cosines;

$$\begin{aligned} r_-^2 &= r^2 + S^2 + 2rS\cos\theta \\ r_+^2 &= r^2 + S^2 - 2rS\cos\theta \ . \end{aligned} \tag{100}$$

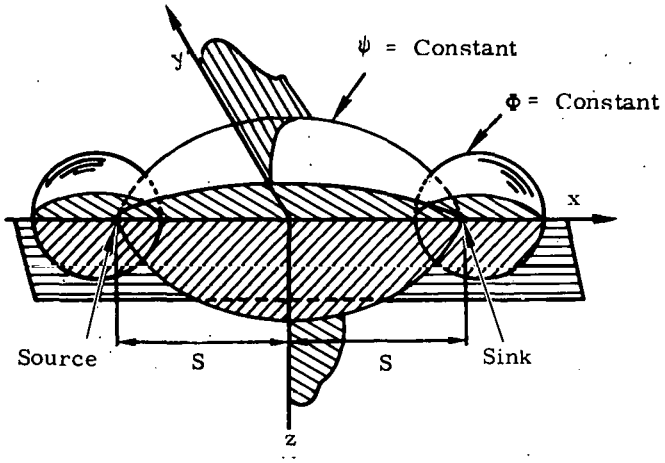

Figure 33. Equipotentials and Stream Surfaces for a Point Source and Sink in an Infinite Permeable Medium

The potential then becomes

$$\Phi(r,\theta) = \frac{Q}{4\pi}\left\{\left(r^2 + S^2 - 2rS\cos\theta\right)^2 - \left(r^2 + S^2 + 2rS\cos\theta\right)^2\right\}^{\frac{1}{2}} \ . \tag{101}$$

The shortest time path for the unconfined configuration is the straight line between $x = \pm S$. The potential along this line becomes

$$\Phi(x) = \frac{Q}{4\pi}\left\{\frac{1}{x+S} + \frac{1}{x-S}\right\} \tag{102}$$

and the velocity in a porous medium along x is

$$V_x = -\frac{1}{\epsilon}\frac{\partial\Phi}{\partial x} = \frac{Q}{4\pi\epsilon}\frac{x^2+S^2}{\left(x^2-S^2\right)^2} \quad . \tag{103}$$

The time of first arrival for isotropic flow is

$$t_{F3} = \frac{2\pi\epsilon}{Q}\int_{-S+a}^{S-a}\frac{\left(x^2-S^2\right)^2}{x^2+S^2}\,dx \tag{104}$$

where a is the radius of the spherical source and sink. If the substitution $u = x/S$ is made and symmetry about $x = 0$ is assumed, Eq. (104) becomes

$$t_{F3} = \frac{2\pi\epsilon S^2}{Q}\int_0^{1-a/S}\frac{(u^2-1)^2}{u^2+1}\,du \quad . \tag{105}$$

After integration,

$$t_{F3} = \frac{2\pi\epsilon S^3}{Q}\left\{\frac{2}{3}\left(1-\frac{a}{S}\right)^3 - 6\left(1-\frac{a}{S}\right) + 8\tan^{-1}\left(1-\frac{a}{S}\right)\right\} \tag{106}$$

$a \ll S$, t_{F3} becomes

$$t_{F3} \approx \frac{2\pi\epsilon S^3}{Q}\left(2\pi + \frac{2}{3} - 6\right) \tag{107}$$

in contrast to the planar flow result of

$$t_F \approx \frac{4}{3}\frac{\pi\epsilon S^2}{q} \quad . \tag{108}$$

The ratio t_{F3}/t_F for equal prefixes is

$$t_{F3}/t_F = 1.425 \tag{109}$$

for $a/S \to 0$.

Because the total flow Q can be measured directly for this configuration, the porosity can be computed using

$$\epsilon = \frac{Qt_{F3}}{2\pi S^3}\left(2\pi + \frac{2}{3} - 6\right) = 0.168\,\frac{Qt_{F3}}{S^3} \quad . \tag{110}$$

The pressure drop can also be calculated for this configuration. It is

$$\Delta P = \left(h_2 - h_1\right)\rho g = \frac{Q\rho g}{2\pi K}\left\{\frac{1}{a} - \frac{1}{2S - a}\right\} \tag{111}$$

where g is acceleration of gravity. With ΔP known, the hydraulic conductivity can be found using Eq (111)

$$K = \frac{Q\rho g}{\pi S \Delta P}\left\{\frac{1 - a/S}{a/S\left(2 - a/S\right)}\right\} \quad . \tag{112}$$

In contrast to the planar flow example, the porosity and hydraulic conductivity can be computed directly using Eqs (110) and (112), respectively, with no prior data reduction and without the use of multiple detectors and a flow-logging injector. However, analysis of three-dimensional tests is limited to formations that are isotropic.

Decay Characteristics of the Recovery Well Pulse

The decay of the recovery-well tracer pulse is not as easy to evaluate as for unconfined planar flow. In fact, it is not possible to express the travel time in a functional form. The inverse velocity was integrated along a streamline numerically. This information was used to plot the relative concentration in the output well as a function of time for a step-function input. The same considerations as in the "Pulse Decay Characteristics ..." section were used to plot Figure 34. The normalized derivative of this curve represents the relative concentration in the output well for a delta function tracer input. This information is displayed in Figure 35.

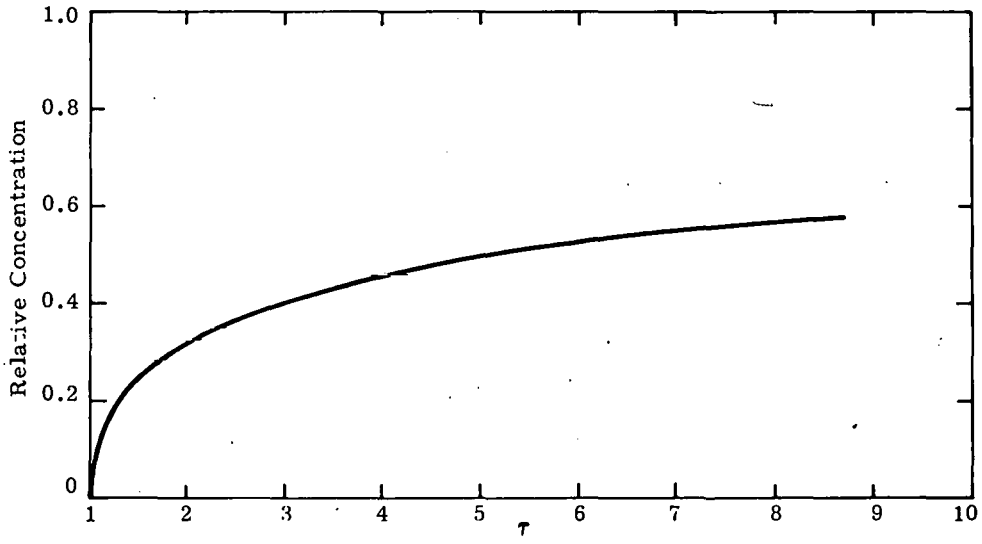

Figure 34. Relative Concentration for Unconfined Three-Dimensional Flow With a Step Input of Tracer

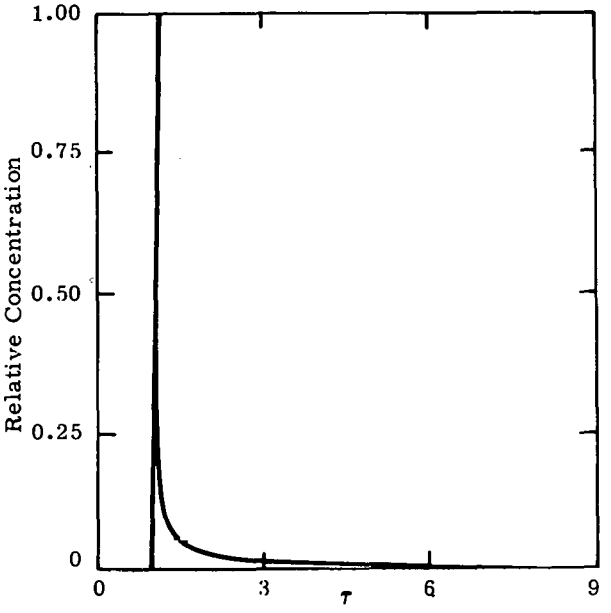

Figure 35. Relative Concentration for Unconfined Three-Dimensional Flow With a Pulse Input of Tracer

Considerable differences exist between these two figures and their equivalents for planar flow (Figure 19). For very short times ($\tau \leq 2$) the decays are faster than the decays of the planar flow patterns. The decay constant in this region is approximately four times that of the planar flow pattern for a pulse input. Attempts to fit Eq (54) to the data in Figure 35 were not successful. The difference in the short time-decay characteristics can be used as an aid to data analysis. If the decay constant of a field test is significantly (a factor of 2) larger than the theoretical two-dimensional unconfined value, the flow is probably three-dimensional and data analysis should proceed accordingly. No other uses for the decay rates were found for three-dimensional flow.

Dispersion

The flow in any plane that contains the x axis can be divided into arcs and dispersion in each arc considered separately. This is the same procedure as used in the "Mechanical Dispersion in Porous Media." For a spherical source and sink it is not possible to present the equation in closed form. The relative dispersion along any stream arc can be represented by

$$C(\tau) = (4\pi\beta\tau/\tau_o)^{-\frac{1}{2}} \exp\left[-(1 - \tau/\tau_o)^2 / 4\beta\tau/\tau_o\right] \qquad (113)$$

where β retains the same meaning as in "Mechanical Dispersion in Porous Media" and τ_o is the nondispersed flow time along that streamline. The relative concentration for any given time τ can be integrated over all streamlines to include the divergence of streamlines. The overall effects of dispersion are much the same as for the planar flow problem. The change in t_{max} as β changes is approximately the same. The major differences are in the long-time ($\tau > 2$) region. For the three-dimensional configuration, the concentration including dispersion stays above the concentration of the divergence-only approximation. Since no data reduction is done in this region, no further work was attempted. One typical dispersive output-well concentration curve is displayed in Figure 36.

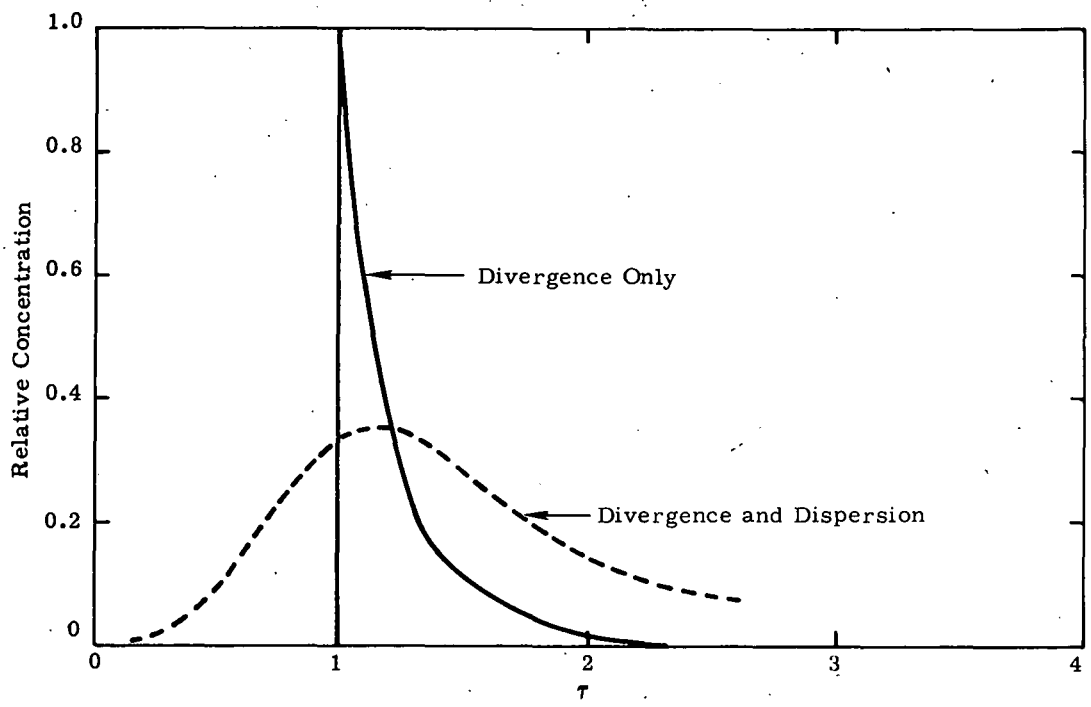

Figure 36. Spreading Due to Dispersion Along Stream Surfaces for $\beta = 0.1$

Comments on Confined Flow

The effects of confinement upon the time of first arrival for three-dimensional flow were not considered. It is possible to construct a velocity potential using spherical sources and sinks in a three-dimensional array, like that of Section IV, for planar flow. The impermeable boundaries would be in the form of a parallelepiped. The size of the confining region and placement of the wells (point sources and sinks) would be variable. It would be possible to construct the streamlines and velocities along these lines. It would also, in theory, be possible to repeat the same calculations done for the planar configuration. It is expected that the trends seen from the planar flow problem would also be repeated in the three-dimensional problem; that is, the time of first arrival would always be shorter for the confined configuration and the largest differences would occur when the well positions approached the boundaries. The unconfined time of first arrival can be considered an upper limit for all experimental values.

VI. Generalizations, Limitations, and Conclusions

Complete flow characterization of all geologic formations cannot be accomplished with existing test methods. Because of the possibility of very complex flow patterns and limited access to the test region, more reliable flow characterization can be obtained by using more than one test method and test configuration. Even then, proper interpretation of test data can be difficult, because several different types of flow nets can result in nearly identical test data. Great care is necessary in test design, data acquisition, data reduction, and data analysis to minimize the possibility of erroneous conclusions. Flow testing difficulties can arise in formations with the following characteristics:

- Discrete fractures that are close together
- Branched fractures
- Unknown confinement of the test region
- Unknown isotropy
- Major flow paths that cannot be intersected by test wells at angles approaching 90°
- Very tight or very loose formations
- Leaky test regions
- Presence of fluids other than the test carrier fluid

The test methods, data reduction, and data analysis described in this report are used to measure porosity and permeability in unconfined isotropic media, and porosity, permeability and fracture characteristics in media with confined or unconfined two-dimensional flow. The following discussion, in conjunction with the equations derived in the body of this report, is intended to aid in designing tests and interpreting data.

The divergence of stream tubes associated with flow between cylindrical or spherical sources and sinks (Figures 18 and 33) converts short rectangular input pulses into exponentially decaying pulses in the output wells (Figures 19b and 35). Since characteristics of the test formation, as well as the test configuration itself, may alter the tracer pulse, the shortest time for any of the tracer pulses to travel through the formation (t_F) is used in most data analyses. In addition to direct measurements, t_F can be computed from the decay constant of the output pulse, using Eqs (56), (57), and (58) for two-dimensional flow. For flow through media with the same porosity and permeability, t_F would be shortest for two-dimensional confined flow, longer for two-dimensional unconfined flow, and longest for three-dimensional unconfined flow (Figure 29 and Eqs (107) and (108)).

Output pulse spreading can be caused by flow through the formation as well as by divergence of streamlines. Although molecular diffusion is negligible, mechanical dispersion can cause spreading on both sides of the peak value (Figure 22). Two-dimensional flow through uniform layers such

as porous or rubbled media (Figure 29) can also cause pulse spreading, but it is in the form of a delay, with the maximum value coming at a time later than t_F (Figure 25). It is usually not possible to distinguish between mechanical dispersion and porous spreading from the output tracer data alone. Porous spreading can produce a longer delay in t_{max} than dispersion, but this delay can be reduced by using small diameter test wells, high flow rates, and large well separations. If the quantity $D/t_F V0$ can be kept below 0.1, t_F can be approximated by $0.9\ t_{max}$ for both types of spreading and it is not necessary to separate the two effects. Flow through a crack produces less pulse spreading than flow through a porous region, but flow logging is necessary to positively identify such a porous region. Increasing the distance between wells elongates the output pulse proportional to S squared, but does not change the relative shape of the curve. Dispersion and flow through porous layers cause the output pulse to be distorted and slightly elongated, and the peak to be delayed.

The decay rate of the output pulse is useful in determining the confinement and isotropy of the test formation. The initial decay rate for a pulse that has passed through a confined region is more rapid than if it had gone through an unconfined region (Figure 31). In addition, the confined pulse has a long, slowly decaying tail. The decay constant for three-dimensional flow (Figure 35) is much larger than for two-dimensional flow (Figure 19b). Regardless of the amount of spreading or the decay rate, the relative transmittance of each flow path for a given test is proportional to the area under its output tracer curve. Because of the importance of the output decay, the output should be recorded for at least 5 τ, or until it has reached background levels.

The streamline plots in Figure 28 and the time plots in Figure 29 are an essential part of the data analysis for confined regions. They are also useful in the design of the experiment by showing the effects of well placement. If tests are made between several well pairs in a confined region, the output of CONFLOW can be used to approximate the boundaries of the region without extensive drilling. Another important application of CONFLOW is in sensitivity studies for systems analyses preceding the design of confined flow processes such as in situ oil shale retorts. Sensitivity studies would show effects of retort shape and well location on flow patterns, transit time, pressure drops and uniformity of flow.

Conducting flow tests in both directions between a well pair can be helpful in locating branched fractures and in defining flow angles between the wells. This can also be accomplished by placing a detector string in the input well. The minimum number of flow paths between sensors is equal to the number of pulses added between the sensors. Superimposed pulses from multiple paths cannot be distinguished from a single pulse by only one test. Resolution can sometimes be improved by repeating the test with the location of the sensor string changed.

Although the test methods, data reduction, and data analysis presented in this report are not applicable to all geologic formations, they do make it possible to characterize fairly complex formations with a reasonable degree of confidence.

References

1. S. W. Lohman, "Groundwater Hydraulics," USGS Professional Paper 708, 1972.

2. S. N. Davis and R. J. M. DeWiest, Hydrogeology (New York: John Wiley & Sons, 1969).

3. A. J. Raudkivi and R. A. Callander, Analysis of Groundwater Flow (New York: John Wiley & Sons, 1976).

4. D. S. Parasnis, Mining Geophysics (New York: Elsevier Scientific Publishing Co., 1975).

5. A. L. Stevens, Oil Shale Programs Fourth Quarterly Report, October 1976 through December 1976, SAND77-0196 (Albuquerque: Sandia Laboratories, 1977).

6. R. R. Boade, ed, Oil Shale Programs Sixth Quarterly Report, April 1977 through June 1977, SAND77-1497 (Albuquerque: Sandia Laboratories, 1977).

7. A. L. Stevens, ed, Oil Shale Programs Fifth Quarterly Report, January 1977 through March 1977, SAND77-2013 (Albuquerque: Sandia Laboratories, 1977).

8. R. R. Boade, ed, Oil Shale Programs Seventh Quarterly Report, July 1977 through September 1977, SAND78-0045 (Albuquerque: Sandia Laboratories, 1978).

9. D. S. Webster, J. F. Procter, and I. W. Marine, "Two-Well Tracer Test in Fractured Crystalline Rock," Geological Survey Water-Supply Paper 1544-I, 1970.

10. P. B. Lorenz, "Radioactive Tracer Pulse Method of Evaluating Fracturing of Underground Oil Shale Formations," Bartlesville Energy Research Center, Report of Investigations 7791, 1973.

11. R. D. Klett, ed, Krypton-85 Disposal Program Semiannual Report - August 15, 1977 to March 31, 1978, SAND78-1667 (Albuquerque: Sandia Laboratories, 1979).

12. R. K. Blankennagel, "Hydraulic Testing Technique of Deep Drill Holes at Pahute Mesa, Nevada Test Site," U.S. Geological Survey Open-File Report, p 50, 1967.

13. R. D. Klett, ed, Krypton-85 Disposal Program Second Semiannual Report - April 1, 1978 to September 30, 1978, SAND79-0398 (Albuquerque: Sandia Laboratories, 1979).

14. R. D. Klett, C. E. Tyner, E. L. Jacobs, and W. C. Riggan, "Geologic Fluid Flow Test System," Record of Invention SD-3857, October 22, 1979.

15. H. E. Thomas, "The Hot Film Flow Log - A Formation Evaluation Tool Designed for Shallow In Situ Oil Shale Experiments," SPE-3501, 46th Annual Fall Meeting, AIME-SPE, New Orleans, LA, October 3-6, 1971.

16. C. E. Tyner, R. D. Jacobson, and P. M. Drozda, "In Situ Oil Shale Retort Characterization With Tracers," to be published.

17. M. Muskat, The Flow of Homogeneous Fluids Through Porous Media (New York: McGraw-Hill Book Co., 1937).

18. D. B. Grove and W. A. Beetem, "Porosity and Dispersion Calculations for a Fractured Carbonate Aquifer Using the Two-Well Tracer Method," Water Resources Research, Vol 7, No. 1, February 1971, pp 128-134.

19. P. V. Danckwerts, "Continuous Flow Systems," Chemical Engineering Science, Vol 2, No. 1, February 1953, pp 1-13.

20. R. H. Perry and C. H. Chilton, Chemical Engineer's Handbook (New York: McGraw-Hill, 1973).

21. J. A. Hoopes and D. R. F. Harleman, "Wastewater Recharge and Dispersion in Porous Media," Journal of the Hydraulics Division, ASCE, Vol. 93, No. HY5, September 1967, pp 51-71.

22. J. A. Hoopes and D. R. F. Harleman, Waste Water Recharge and Dispersion in Porous Media, Report No. 75 (Cambridge: Hydrodynamics Laboratory, MIT, June 1965).

23. M. S. Hantush and C. E. Jacob, "Plane Potential Flow of Groundwater with Linear Leakage," Transactions of the American Geophysical Union, Vol. 35, No. 6, December 1954, pp 917-936.

24. E. S. Hertel, Jr, CONFLOW, A Computer Code Describing Flow Between Two Wells in a Confined Region, SAND80-1645 (Albuquerque: Sandia National Laboratories, April 1981).

Glossary

Active Void	Total void volume of a flow path less stagnant regions and closed cells.
Dispersion	Hydrodynamic spreading of a tracer pulse parallel to streamlines. It is caused by different mechanical flow paths in a media.
Divergence	The variation in width and length of diverging/converging stream tubes for flow between cylindrical or spherical sources and sinks. This causes a delta input tracer pulse to be converted to an exponentially decaying output pulse.

NOMENCLATURE

A_i'	Cross-sectional area available for flow between regions i and i-1 (m^2)
A_i''	Cross-sectional area available for flow at detector i (m^2)
a	Radius of wells
$a(\alpha)$	Relative transit time as a function of α
B_T	Total tracer injected (Ci)
B_{fT}	Total tracer injected during flow test (Ci)
$D_i(t)$	Rate of tracer passing detector i (Ci/s)
$b_i(t)$	Rate of tracer arrival in region i (Ci/s)
$b_i^j(t)$	Rate of tracer arrival in region i on path j (Ci/s)
$b_{fi}(t)$	Rate of tracer arrival in region i during flow test (Ci/s)
b_{fiT}	$\int_o^\infty b_{fi}(t)dt$ total tracer entering region i during flow test (Ci)
c_i	Calibration factor for i^{th} detector (Ci-s/m^3 · counts)
C_o	Relative concentration constant for pulse spreading of unconfined flow
C(t)	Relative concentration of tracer in the discharge well (just above the flow path) as a function of time
C_i'	Probability of radioactive decay being counted (counts/decay)
C_t	Probability of radioactive decay (decays/Ci · s)
D	Thickness of the permeable region
DE	Equivalent pipe diameter
d_i	Distance between detectors i and i-1 (m)
f	Fanning friction factor
f'	Modified friction factor (Reference 20)
G	Mass velocity ($V\rho$)
g	Gravitational constant
h	Thickness of fracture
K	Hydraulic conductivity = $k\frac{\rho g}{\mu}$
k	Intrinsic permeability or number of regions of injection well

L	Length
L_H	Half-length of the bounded-flow region
ℓ_i	Length of detector i (m)
M	Mass of tracer injected
MAT_i^j	Mean arrival time of tracer along j^{th} path into region i(s)
M_m	Mean molecular weight
MWT_i	Injection wellbore transit time (s)
m	y integer position parameter for the confined region
n	Granular media exponent (Reference 20) or x integer position parameter for the confined region
n1, n2	Integer position parameters for the infinite strip
N	Frictional resistance, fL/R_H
$N_i(t)$	Count rate above background at detector i (counts/s)
N_{iT}	$\int_o^\infty N_i(t)\,dt$ total number of counts above background by detector i (counts)
$N_i'(t)$	Count rate at detector i (counts/s)
$N_{fi}(t)$	Count rates at detector i during flow test (counts/s)
N_{fiT}	$\int_o^\infty N_{fi}(t)\,dt$ total number of counts at detector i during flow test (counts)
NB_i	Background count rate at detector i (counts/s)
P	Pressure
P_i	Probability of decaying atoms being detected (counts/Ci)
P_{inj}	Injection-well pressure (Pa)
P_m	Mean-formation pressure (Pa)
P_o	Standard pressure (1.01×10^5 Pa)
P_r	Recovery-well pressure (Pa)
Q	Total volumetric flow rate
Q_i	Flow rate past detector i (m^3/s)
Q_{inj}	Flow rate into injection well (m^3/s)
$Q_{inj}^{k'}$	Flow rate at region k' of injection well (m^3/s)
q	Volumetric flow rate through formation/unit hole length
q_i	Flow rate into Region i (m^3/s)
q_i^j	Flow rate into Region i along path j (m^3/s)

R	Gas constant
R_H	Hydraulic radius
r	Radius or position vector from the coordinate origin
r_+	Position vector for the sink
r_-	Position vector for the source
S	Half the well separation
T	Temperature
T_{inj}	Injection-well temperature (K)
T_{in}	Mean formation temperature (K)
T_o	Standard temperature (273 K)
t	Time (s)
t_F	Time of first arrival for a negligible well radius
t_{FC}	Time of first arrival of tracer for the confined region
t_{F3}	Time of first arrival of a tracer for spherical sources and sinks
t_{max}	Time of maximum concentration
$t(\alpha)$	Transit time along streamline α
ℓ_i	Time for flow from detector i-1 to i (s)
u_τ	The relative distance a plug of tracer would move down the wellbore of a permeable region as a function of τ
V	Velocity
VD	Flow velocity at the bottom of a permeable region
V_x	Flow velocity in the $\hat{x}$ direction
V_y	Flow velocity in the $\hat{y}$ direction
V_z	Flow velocity in the $\hat{z}$ direction
V0	Flow velocity at the top of a permeable region
v_i	Volume of recovery well between detectors i and i-1 (m^3)
v_i'	Volume of hardware between detectors i and i-1 (m^3)
v_j	Active void along path j in Region i (m^3)
$v_w^{k'}$	Void volume of injection well in Region k (m^3)
W_H	Half-width of the bounded flow region
x1, y1	Coordinates of the input well
x2, y2	Coordinates of the output well
Y1, Y2	Image position functions for an infinite bound strip
Z	Compressibility

α	$\beta_2 - \beta_1 - \pi$ angle that identifies streamlines for the unconfined source sink (see Figure 18)
β	Dispersion constant
γ	Specific heat ratio (C_P / C_V)
ϵ	Porosity
ζ	Complex potential
Θ	Shape factor of granules (Reference 20)
η	A function including a, S, and $(\Delta P_c / \Delta P_u)$
θ	The angle between r and z
θ_i	Time atom remains in vicinity of detector (s)
λ	Decay constant for pulse spreading of unconfined flow
μ	Viscosity
$\xi(t)$	An angular function that expresses a stream angle (α) with transit time equal to t
ρ	Carrier-fluid density
σ	The full width of half maximum of a concentration curve
$\sigma(\alpha)$	Gaussian population variance as a function of α
τ	Time relative to the appropriate time of first arrival
τ_o	Nondispersive transit time along any streamline
Φ	Velocity potential
Ψ	Stream function

Subscripts

c	Confined
f	Flow test value
i	Region index
n	Number of regions
u	Unconfined

Superscripts

j	Index of path number within region

DISTRIBUTION:

Fenix & Scisson, Inc.
PO Box 498
Mercury, NV 89203
Attn: F. D. Waltman

State of Nevada
Capitol Complex
Carson City, NV 89710
Attn: N. Clark, Dept of Energy

International Atomic Energy Agency
Div of Nucl Power & Reactors
Karntner Ring 11
PO Box 590, A-1011
Vienna, Austria
Attn: J. P. Colton

Fenix & Scisson, Inc.
PO Box 15408
Las Vegas, NV 89114
Attn: G. Pinder

University of California (5)
Lawrence Berkeley Laboratory
Energy & Environment Division
Berkeley, CA 94270
Attn: P. Witherspoon
C. Fu Tsang
M. J. Lippmann
T. Chan
K. Pruess

Hanford Eng Development Lab
PO Box 1970
Richland, WA 99352
Attn: D. Cantley

Arthur D. Little, Inc.
Acorn Park
Cambridge, MA 02140
Attn: C. R. Hadlock

Texas A&M University
Center for Tectonophysics
College Station, TX 77840
Attn: J. Handin

Holmes & Narver, Inc.
PO Box 1
Mercury, NV 89023
Attn: G. E. Christensen

Dept of Health and Environment
Bureau of Radiation Control
Forbes Field
Topeka, KS 66620
Attn: G. W. Allen, Director

Kaiser Engineers
300 Lakeside Drive
Oakland, CA 94666
Attn: H. Julien

Dames & Moore (2)
Advanced Technology Group
44 Mall Road
Burlington, MA 01803
Attn: G. Hooking
P. Huyahorn

Radiation Protection Div
1000 Northeast 10th Street
PO Box 53551
Oklahoma City, OK 73152
Attn: R. L. Craig, Dir

University of Texas at Austin
University Station, Box X
Austin, TX 78712
Attn: E. G. Wermund

Exxon Nucl Idaho Co, Inc (4)
550 Second St
Idaho Falls, ID 83401
Attn: R. Brown (2)
Gaseous Wastes & Geothermal Sec
D. Knecht (2)
Krypton Storage Div

Battelle Pacific Northwest Lab (3)
PO Box 999
Richland, WA 99352
Attn: G. Tingey (2)
R. A. McCann

Environmental Program Supervisor
903 Ninth Street Office Bldg
Richmond, VA 23219
Attn: K. J. Buttleman

Energy Administration
Dept of Natural Resources
Tawes State Office Bldg
Annapolis, MD 21401
Attn: P. Massicot, Actg Dir

Radiation Health Info Project
Environmental Policy Inst
317 Pennsylvania Ave, SE
Washington, DC 20003
Attn: E. Walters

University of New Mexico
Dept of Chemical and Nucl Eng
Albuquerque, NM 87131
Attn: H. E. Nuttall

DISTRIBUTION (Cont):

Rockwell Hanford Operations (6)
PO Box 800
Richland, WA 99352
Attn: R. E. Smith
Commercial Waste & Spent
Fuel Packaging Prog Mgr
W. J. Kurzecka
Commercial Waste Mgr
L. L. Tignac
K. H. Henry
R. Deju
B. Dietz

Oak Ridge National Laboratory
PO Box X
Oak Ridge, TN 37830
Attn: H. O. Weeren

George Fumich, Jr, Secretary
for Fossil Energy
Mail Stop B-127
Washington, DC 20545

US Department of Energy (10)
Office of Deputy Assistant
Secretary, Oil, Gas, and Shale
Technology
Mail Stop D-107
Washington, DC 20545
Attn: M. Adams
B. Harney
J. B. Smith
A. M. Hartstein
P. R. Wieber
J. W. Ramsey
H. E. Thomas
E. L. Burwell
R. W. Markley
D. Uthis

Laramie Energy Technology Center (9)
PO Box 3395, University Station
Laramie, WY 82071
Attn: R. J. Jacoletti
J. H. Weber
W. E. Little
B. C. Sudduth
L. P. Jackson
D. R. Johnson
A. E. Harak
R. E. Poulson
T. F. Turner

Los Alamos National Lab (10)
PO Box 1663
Los Alamos, NM 87545
Attn: K. Wolfsberg (2)
L. S. Germain, M/S 570
L. Lanham, M/S 755
B. M. Crowe, M/S 978
W. J. Carter, M/S 329
J. N. Johnson, M/S 214
C. L. Edwards, M/S 329
C. A. Anderson
R. J. Bridewell

Lawrence Livermore Laboratory (14)
PO Box 808
Livermore, CA 94550
Attn: L. D. Ramspott, L-204
A. Holzer, L-209
L. B. Ballou, L-204
J. S. Kahn, L-49
K. Street, L-209
R. C. Carlson, L-204
A. B. Miller, L-204
J. A. Karver
J. Parlegreco
A. E. Lewis
J. H. Campbell
J. F. Carley
R. J. Lytle
W. Dailey

Science Applications, Inc (2)
1546 Cole Blvd
Suite 210
Golden, CO 80401
Attn: H. E. McCarthy
G. B. French

Southwest Research Institute (2)
6220 Culebra Road
PO Drawer 28510
San Antonio, TX 78284
Attn: T. E. Owen
B. M. Duff

Blastmasters, Inc
325 Beverly Avenue
San Leandro, CA 94577
Attn: K. Britton

US Bureau of Mines - Twin Cities (2)
PO Box 1660
Twin Cities Airport, MN 55111
Attn: R. Thill
S. Demou

DISTRIBUTION (Cont):

Rio Blanco Oil Shale Co
9725 E. Hampden Ave
Denver, CO 80231
Attn: J. Knepper

Science Applications, Inc
PO Box 273
Steamboat Springs, CO 81047
Attn: C. Young

Occidental Research Corp (5)
2100 SE Main Street
PO Box 19601
Irvine, CA 92713
Attn: D. C. Chang
W. McDermott
R. Nelson
J. Feinman
R. Bloom

Occidental Oil Shale, Inc (3)
751 Horizon Drive
Box 2687
Grand Junction, CO 81501
Attn: R. Ellender
G. Gruber
T. Ricketts

Equity Oil Company
10 W. Third South
Suite 806
Salt Lake City, UT 84101
Attn: P. M. Dougan

Geokinetics, Inc
280 Buchanan Field Rd
Concord, CA 94520
Attn: M. Lekas

Rocky Mountain Energy Co
Lakeside National Bank Bldg
4707 Harlan Street
Denver, CO 80212
Attn: T. I. Sharps

US Department of Energy
Asst Secretary for Nuclear Energy
Mail Stop GE-095
Washington, DC 20545
Attn: G. W. Cunningham, NE-1

US Department of Energy
Idaho Operations Office
Nuclear Fuel Cycle Division
550 Second St.
Idaho Falls, ID 83401
Attn: J. B. Whitsett

US Department of Energy (2)
Richland Operations Office
PO Box 550
Richland, WA 99352
Attn: F. Standerfer
D. J. Squires

US Department of Energy
Albuquerque Operations Office
PO Box 5400
Albuquerque, NM 87185
Attn: D. T. Schueler, Jr

US Department of Energy
San Francisco Operations Office
1333 Broadway, Wells Fargo Bldg
Oakland, CA 94612
Attn: L. Lanni

The Aerospace Corporation
2350 E. El Segundo
El Segundo, CA 90009

Carbondale Mining Technology Centers
PO Box 2587
Carbondale, IL 69201
Attn: T. Ziegler

US Department of Energy, Hqs (14)
Washington, DC 20545
Attn: Division of Waste Products
G. K. Oertel, Director
G. H. Daly, Chief Tech Br
J. C. Dempsey, Tech Br (5)
D. J. McGoff, Operations Br
Division of Waste Isolation
C. R. Cooly, Chief R&D Br (2)
C. H. George, Chief Geol Ex Br (2)
D. L. Vieth, Chief Proj Br (2)

US Department of Energy (4)
Nevada Operations Office
PO Box 14100
Las Vegas, NV 89114
Attn: R. M. Nelson (2)
R. R. Loux (2)

US Department of Energy (3)
NTS Support Office
PO Box 435
Mercury, NV 89023
Attn: J. H. Dryden
F. Huckabee
L. P. Skousen

Nuclear Regulatory Commission (2)
Washington, DC 20555
Attn: J. C. Malaro, M/S SS674
R. Boyle, M/S P-522

DISTRIBUTION (Cont):

Holmes & Narver, Inc
PO Box 14340
Las Vegas, NV 89114
Attn: A. E. Gurrola

Westinghouse
PO Box 708
Mercury, NV 89023
Attn: D. C. Durrill

Westinghouse - AESDV (6)
PO Box 10864
Pittsburgh, PA 15236
Attn: J. B. Wright
W. R. Morris
T. E. Cross
R. J. Bahorich
C. R. Bolugren
W. A. Henninger

US Geologic Survey (3)
National Center
Reston, VA 22092
Attn: G. D. DeBuchananne, M/S 410
P. R. Stevens, M/S 410
D. B. Stewart, M/S 959

US Geologic Survey (2)
PO Box 25046
Federal Center
Denver, CO 80225
Attn: G. L. Dixon, M/S 954
W. S. Twenhofel, M/S 954

Geologic Society of America
3300 Penrose Place
Boulder, CO 80302
Attn: J. C. Frye

Battelle Memorial Institute (13)
Office of Nucl Waste Isolation
505 King Avenue
Columbus, OH 43201
Attn: N. E. Carter
S. Basham
J. Carr
ONWI Library (5)
R. A. Robinson
W. Carbiener
H. C. Burkholder (2)
J. D. Waddell

State of Nevada
Governor's Office of Planning Coordination
Capitol Complex
Carson City, NV 89710
Attn: R. Hill, State Planning Coordinator

The Dikewood Corp (2)
16B University, NE
Albuquerque, NM 87106
Attn: L. W. Davis

Martin Marietta Laboratories
1450 South Rolling Road
Baltimore, MD 21227
Attn: S. Winzer

1000 G. A. Fowler
1100 C. D. Broyles
1110 J. D. Plimpton
1116 R. P. Reed
1116 C. W. Cook
1120 T. L. Pace
1123 B. C. Benjamin
1124 J. W. Wistor
1125 G. L. Ogle
1130 H. E. Viney
1133 R. D. Statler
1133 W. C. Wilson
1137 C. D. Northam
2351 W. C. Riggan
2510 D. H. Anderson
2514 P. J. Langdon
2533 E. F. Richardson
3151 A. A. McConnell
4000 A. Narath
4400 A. W. Snyder
4500 E. H. Beckner
4510 W. D. Weart
4511 D. D. Gonzalez
4530 R. W. Lynch
4531 L. W. Scully
4536 D. R. Anderson
4536 E. S. Hertel (30)
4536 R. D. Klett (10)
4537 L. D. Tyler
4537 J. K. Johnstone
4537 B. S. Langkopf
4537 A. R. Lappin
4537 D. R. Waymire
4537 R. M. Zimmerman
4538 R. C. Lincoln
4540 M. L. Kramm
4543 J. F. Ney
4550 R. M. Jefferson
4700 J. H. Scott
4710 G. E. Brandvold
4717 R. R. Neel
4740 R. K. Traeger
4742 A. F. Veneruso
4746 B. Granoff
4747 D. W. Cook
4747 R. R. Boade
4747 J. T. Schamaun

DISTRIBUTION (Cont):

4747 C. E. Tyner
4747 P. J. Hommert
4748 P. M. Drozda
4748 R. D. Jacobson
4748 R. L. Parrish
4748 J. E. Uhl
4748 B. E. Bader
4753 D. A. Northrop
4754 C. L. Schuster
4754 L. K. Warne
4755 R. L. Fox
4756 H. M. Dodd
5000 J. K. Galt
5100 F. L. Vook
5500 O. E. Jones
5510 D. B. Hayes
5511 J. W. Nunziato
5511 D. C. Reda
5512 D. F. McVey
5513 D. W. Larson
5520 T. B. Lane
5521 R. K. Thomas
5530 W. Herrmann
5532 B. M. Butcher
5541 W. C. Luth
5541 J. L. Krumhansl
8214 M. A. Pound
3141 L. J. Erickson (5)
3151 W. L. Garner (3)
For DOE/TIC (Unlimited Release)
DOE/TIC (25)
(J. Hernandez, 3154-4)

☆U.S. GOVERNMENT PRINTING OFFICE: 1981-0-777-023/568

Org.	Bldg.	Name	Rec'd by *	Org.	Bldg.	Name	Rec'd by *